Universidad de La Laguna

Facultad de Ciencias
Sección de Física

Bachelor's Thesis

Characterizing the properties of a MoSi Superconducting Single Photon Detector

Rafael Luque Merino

Supervisor:
Dr. Víctor Lavín della Ventura

Abstract

In this thesis, we examine the properties of a MoSi superconducting nanowire single photon detector. MoSi is a promising material in the field of quantum optics apliccations, due to its amorphous structure and low energy gap, compared to conventional crystalline NbN. We characterize the superconducting properties of the detector, finding a superconducting critical temperature of $T_c = 4.98\ K$ and a critical current at 0 K of $I_c(0) = 30.91\ \mu A$. The I-V curves of this MoSi nanodetector are similar to those of similar devices fabricated in NbN. We also present experimental results on the photon counting properties of the device, achieving a maximum count rate of 6 MHz, with a relative low dark count rate. At the base temperature of $T = 3.35\ K$, the critical current of the nanodetector was $I_c = 6\ \mu A$. The count rate shows qualitative differences compared to other works with MoSi single photon detectors, but this result is not conclusive. Lastly, we present a modified Quantum Detector Tomography protocol to obtain the intrinsic response of this detector, as well as two experimental setup improvements that enhance the implementation of Quantum Detector Tomography. Understanding the properties and detection mechanism of superconducting nanowiresingle photon detectors (SNSPD's) will contribute to the development of new technologies.

Resumen

Caracterizamos las propiedades de un detector de foton único de nanocable superconductor fabricado en MoSi, un material superconductor amorfo. En estos detectores, los fotones inciden sobre dicho nanocable rompiendo su estado superconductor. Esto genera un pulso de voltaje que constituye una 'detección de fotón'. Se estudian las propiedades superconductoras del detector, cuya temperatura crítica superconductora es $T_c = 4.98\ K$. La corriente crítica a 0 Kelvin del nanodetector es $I_c(0) = 30.91\ \mu A$. Se estudian las curvas características I-V para comprobar el comportamiento superconductor, comparándolas con las obtenidas en un nanodetector similar fabricado en NbN. Se estudia el ritmo de cuentas (detecciones de fotón) del nanodetector, en función de la corriente aplicada y la potencia óptica incidente. La frecuencia máxima obtenida es de 6 MHz. La corriente crítica superconductora del nanodetector es $I_c = 6\ \mu A$, para una temperatura de $T = 3.35\ K$. Comparamos el rendimiento detectando fotones únicos de este detector con otros nanodetectores similares. Finalmente, presentamos la técnica de Tomografía Cuántica de Detectores con la que podemos caracterizar la respuesta completa de este nanodetector. Se realizan las medidas experimentales necesarias para aplicar este método y se proponen dos mejoras al montaje experimental, con el fin de aumentar la precisión del método tomográfico. Obtener la respuesta intrínseca de estos detectores de fotón único es clave hacia la comprensión del mecanismo físico por el que se produce la detección. Esto a su vez, permitirá diseñar y fabricar detectores más eficientes para diversas aplicaciones tecnológicas.

Contents

1. Introducción

La detección de luz ha sido un tema de gran interés en la física del último siglo, siendo una herramienta necesaria a la hora de medir propiedades de sistemas muy diversos. Detectar luz con precisión y fiabilidad es de suma importancia en aplicaciones de caracter científico (obtener mejores instrumentos de medida) y de carácter tecnológico, con una gran variedad de sensores y aparatos que hoy aparecen en nuestro vida cotidiana. Hoy en día, el reto es detectar luz en su expresión fundamental, el fotón o cuanto de la radiación electromagnética. Un fotón es un sistema puramente cuántico por lo que este desafío cae dentro del campo de la óptica cuántica, en la que nos apoyaremos para desarrollar este proyecto. Actualmente existe una gran demanda de instrumentación que permita detectar un único fotón con gran resolución temporal y espacial, para su aplicación en avances tecnológicos como la criptografía cuántica (o Quantum Key Distribution) [1], la comunicación óptica a través del espacio [2, 3], mejoras en la adquisición de imágenes médicas [4] o el campo de la información cuántica [5].

En este trabajo caracterizaremos un tipo de detector de fotón único, basado en un cable de dimensiones nanométricas que colocamos en un estado superconductor. Al mantener este cable ligeramente por debajo de su corriente crítica superconductora, la llegada de uno o más fotones puede romper el estado superconductor del material, generando un cambio medible en nuestro circuito que definiremos como ”detección de un fotón”. Este tipo de detectores, conocidos como SNSPD, ofrecen una eficiencia de detección alta [6], un nivel bajo de cuentas oscuras (o falsas cuentas), un amplio rango de longitudes de onda y otras propiedades deseables como un tiempo corto de reseteo. Esto los convierte en grandes candidatos para las aplicaciones nombradas anteriormente. Generalmente este tipo de detectores han sido fabricados en NbN, un superconductor cristalino convenciona. También se han desarrollado estos detectores utilizando WSi [7], MoGe [8], MoSi [9, 10, 11, 12] o NbTiN [13, 14]. En este proyecto, utilizaremos un SNSPD fabricado de MoSi, el cual es un superconductor de estructura amorfa, a diferencia del NbN. Además, dispondremos de un detector muy similar fabricado en NbN, con el fin de comparar sus propiedades.

Es importante señalar que el mecanismo de detección, el proceso físico mediante el cual la energía del fotón rompe el estado superconductor, no se entiende completamente [15, 16]. Distintos materiales y diseños de fabricación de estos detectores señalan a distintos modelos de detección existentes [17, 18, 19, 20, 21]. La geometría de los dos detectores utilizados en este trabajo está diseñada con el objetivo de localizar las detecciones de fotón y comprender sus mecanismos físicos [15, 22]. Con el fin de caracterizar la respuesta

intrínseca del detector, se aplica la técnica de Tomografía Cuántica de Detectores. Este método matemático permite obtener la respuesta completa del nanodetector, incidiendo con pulsos coherentes de luz generados por un láser. Ajustaremos los datos a una función tomográfica que relaciona la base de estados coherentes$|\alpha\rangle$ con la base de Fock $|i\rangle$(o base de número de fotones), para así obtener la respuesta intrínseca del detector. El objetivo de este trabajo es: caracterizar las propiedades superconductoras de nuestro detector de fotón único fabricado en MoSi, comparar su rendimiento contando fotones con el de un detector de NbN y con trabajos anteriores realizados con detectores de MoSi. Se muestra la técnica de Tomografía Cuántica de Detector, y se describen dos mejoras al montaje experimental utilizado en la tomografía.

1 Introduction

Detecting light has been one of the most prominent topics in Physics over the last century. Many applications have been realized using the classical treatment of light, but the current challenge is to control and manipulate light at its fundamental quantum level. This lies in the field of Quantum Optics. Light detectors capable of resolving a single photon are the main topic of this work. Since the first demonstration by Golt'smann in 2011 [23], Superconducting Single Photon Detectors (SSPD) are a prime candidate for quantum optics applications because they combine a very high detection efficiency with high counting speed (of the order of GHz). Applications include technological breakthroughs such as quantum key distribution (QKD) [1], quantum information [5], free space communications [2] or medical imaging developments [4].

The main advantages of these detectors are their low dark count rate, high detection efficiency, broad wavelength range (up to mid-infrared), very low timing jitter and short reset time [6]. Compared to other technologies used to detect single photons, these devices use two main features: superconductivity and a nanoscale structure. A SSPD typically detects single photons when operated in the superconducting state and biased just below its critical current I_c. The arrival of a photon breaks the superconducting state and leads to a measurable change in the circuit, in the form of a voltage pulse that represents a 'detection event'. To date, most SSPD's have been fabricated in NbN, but they have been realized in other superconductors such as WSi [7], MoGe [8, 24], MoSi [9, 10, 11] or NbTiN [13, 14].

We will work with a superconducting nanowire single photon detector fabricated in MoSi. This is an amorphous superconductor, structurally different to crystalline superconductors such as NbN. Amorphous superconductors make the fabrication of the detectors much less restrictive on the substrate, temperature and sputtering conditions of the material. MoSi also a lower superconducting gap and lower critical current density than NbN. Superconducting single photon detectors based on amorphous materials seem to yield higher efficiencies, as a qualitative difference in the efficiency as a function of photon energy has

been observed [25, 26]. The reasons for this discrepancy between MoSi [25] and NbN [26] are still unknown. It should be stated that these results were obtained using different device geometries, which could be responsible for differences in the outcome of the experiments. To account for this, we will study a MoSi nanodetector with a geometry analogous to the NbN detector used in Ref. [26] and also compare it with earlier results on MoSi nanodetector with a different geometry.

The geometry of our detector is based around a nanoconstriction, a wedge in the nanowire. This constriction is the most narrow area of the detector (150 nm wide), therefore having the highest critical current density. This makes the nanoconstriction the most efficient part of the detector and we will usually regard it as the only active area. These detectors, called Superconducting Nanowire Single Photon Detectors (SNSPD), are ideal for measuring multi-photon events and exploring the underlying mechanism that causes the energy of the photon to break the superconducting state. This is an important question, as understanding which is the underlying process behind photon detection will help designing and fabricating faster and more efficient single photon detectors.

The goal of this thesis is to characterize the superconducting properties of a MoSi thin film nanodetector, measure its photon counting properties and comparing them to earlier results. Quantum Detector Tomography (QDT) is needed to obtain and quantify the response of our SNSPD. We present this technique and implement changes in the experimental setup in order to enhance QDT. Previous research conducted at Leiden University [26] has shown this is an essential step towards testing the current models on the detection mechanism for these devices.

2. Metodología experimental

A continuación, se presentan los métodos experimentales utilizados en este proyecto. Comenzamos describiendo los detectores de fotón único que utilizaremos, uno de un superconductor amorfo como MoSi, y otro de NbN, un material superconductor cristalino utilizado ampliamente en este campo. Ambos detectores tienen una geometría de nanoconstricción. El nanocable por el que circula corriente y donde inciden los fotones, tiene un estrechamiento que constituye la zona activa del detector. Esto se debe a la elevada densidad de corriente en esta constricción. La principal ventaja de dicha geometría es que podemos localizar las detecciones de fotón para investigar qué procesos intervienen en ellas. Además, como la zona activa es muy reducida, aumentan nuestras posibilidades de observar eventos de detección de varios fotones cercanos.

El objetivo principal del experimento es iluminar el detector con luz coherente y registrar su respuesta como pulsos de voltaje que representan fotones detectados. El montaje experimental consiste de dos partes bien diferenciadas, el montaje óptico y el circuito eléctrico. En el montaje óptico, el objetivo será dirigir la iluminación del láser hacia el detector, y controlar la misma utilizando una serie de atenuadores, espejos y lentes. Así mismo, se usa un prisma para obtener rayos secundarios con los que caracterizar en tiempo real la potencia del láser incidente. El circuito eléctrico alimenta al nanodetector con una corriente continua, cerca de la corriente crítica superconductora I_c; a la vez que registra la detección de fotones como pulsos de corriente alterna, que dirigiremos a una cadena de amplificadores. El detector de fotón único se modeliza como un interruptor en paralelo con una resistencia, donde la posición cerrado representa el estado superconductor y la posición abierta representa el estado normal resistivo del aparato.

Finalmente, se introduce la Tomografía Cuántica de Detectores como un método matemático que permite caracterizar la respuesta completa del detector. Éste método se basa en relacionar la respuesta del detector a estados coherentes con la respuesta a estados de Fock, estados cuánticos con un número medio de fotones bien definido. Además, se modifica este método para facilitar su implementación, agrupando todas las fuentes de atenuación en un único parámetro η. Esto reduce enormemente la complejidad del análisis tomográfico.

2 Setup and methods

2.1 Superconducting nanodetectors

In this thesis, we will work with amorphous MoSi and crystalline NbN based single photon detectors. The geometry of these detectors features a nanoconstriction where the highest current density is concentrated. This constriction is by far the most sensitive area of the SNSPD and we can assume all detection events happening in this active area [27]. These nanodetectors detect single photons when they are biased near their superconducting critical current. In this situation, an inciding photon can break the superconducting state with its energy, generating a pulse that constitutes a 'detection event'. The NbN detector has an active area of 150 x 150 nm and 5 nm thickness. The studied MoSi nanodetector has an active area of 210 x 150 nm and it is 4.5 nm thick. Localizing all detection events improves the chances of observing multi-photon events, in which more than one photon hit the nanowire close in both time and space. These multi-photon events give us information about the response of the detector as a function of the total absorbed energy [26, 28]. We will present a tomographic method to investigate the intrinsic response of the detector, as well as the underlying mechanism of photon counting.

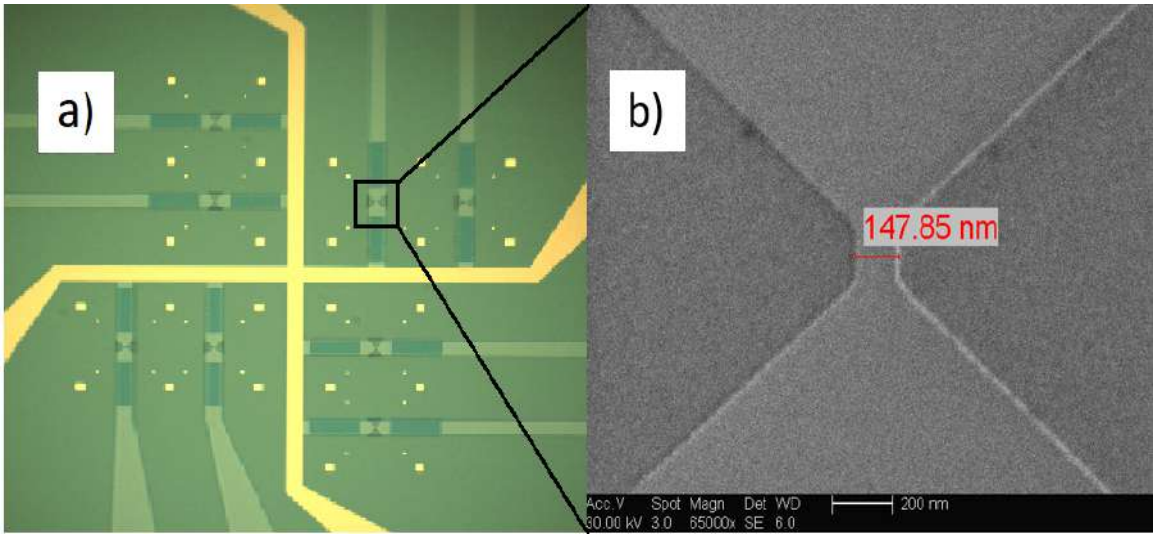

Figure 2.1: Superconducting MoSi nanodetectors. a) Microscopic image of a chip carrier with 8 detectors b) SEM image of the 150 nm wide nanoconstriction. Images provided by V. Verma, NIST (Boulder, EEUU)

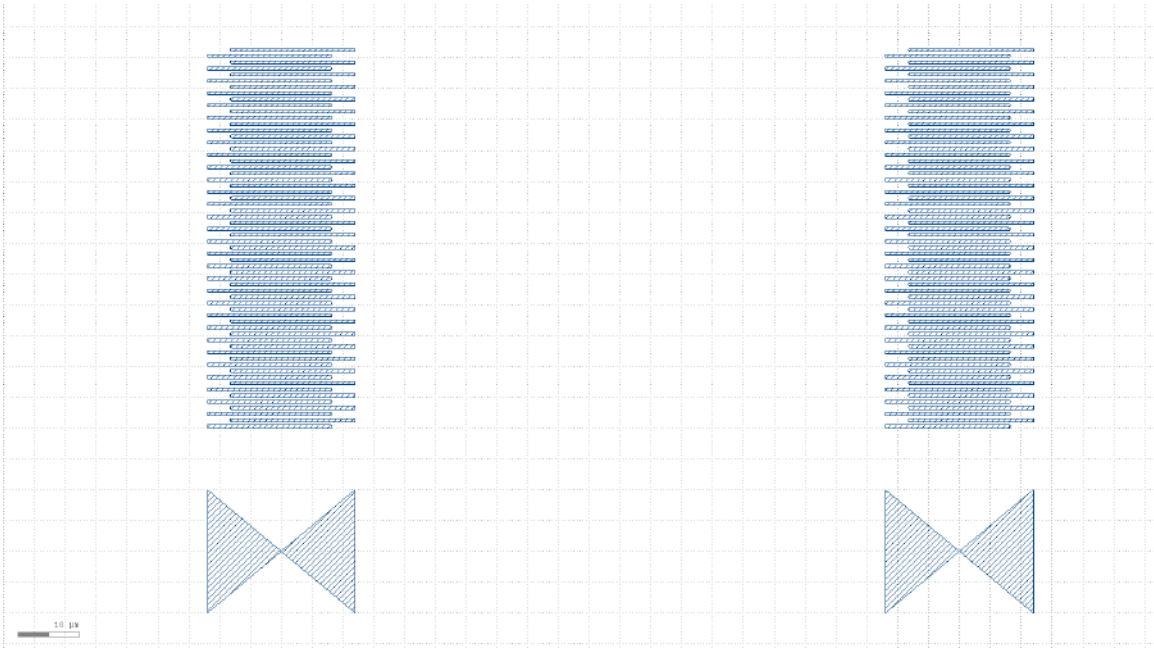

Figure 2.2: Layout used in the design of the MoSi nanodetectors, illustrating the relative dimensions of the meanders. Image provided by V. Verma, NIST (Boulder, EEUU

Figure 2.1 shows an optical microscope image of a chip with 8 MoSi nanodetectors (left) and a SEM image of the $150\ nm$ wide detector (right). In the first image, the nanodetectors can be seen as triangular constrictions around the yellow cross. This cross serves a gold contact pads, that we use to put current through the detectors. The MoSi film was sputtered on top of a Si wafer, with a SiO_2 layer beneath it. In Figure 2.2 we can see the layout for the design of two MoSi nanodetectors, consisting of two meanders and the nanoconstriction or active area. The meander are long zig-zag loops of the same nanowire which act as a coil. Two meandersare added to increase the inductance of the device, in order to avoid a very short reset time that could cause latching of the detector. [29]. These devices were fabricated by Varum Verma at NIST (Boulder, EEUU). More information on the fabrication of similar MoSi nanodetectors is available in Refs. [8, 11, 9, 12]

2.2 Optical setup

The main goal of the experiment is to characterize the response of the detector, using a range of coherent states. These states are prepared by attenuation of the laser beam, that is then directed into the single photon detector, which is put inside a cryostat. The main quantities under study are: i) the count rate of the detector, ii) the optical power on the detector. The current through the detector is also controlled, using the electric setup. Figure

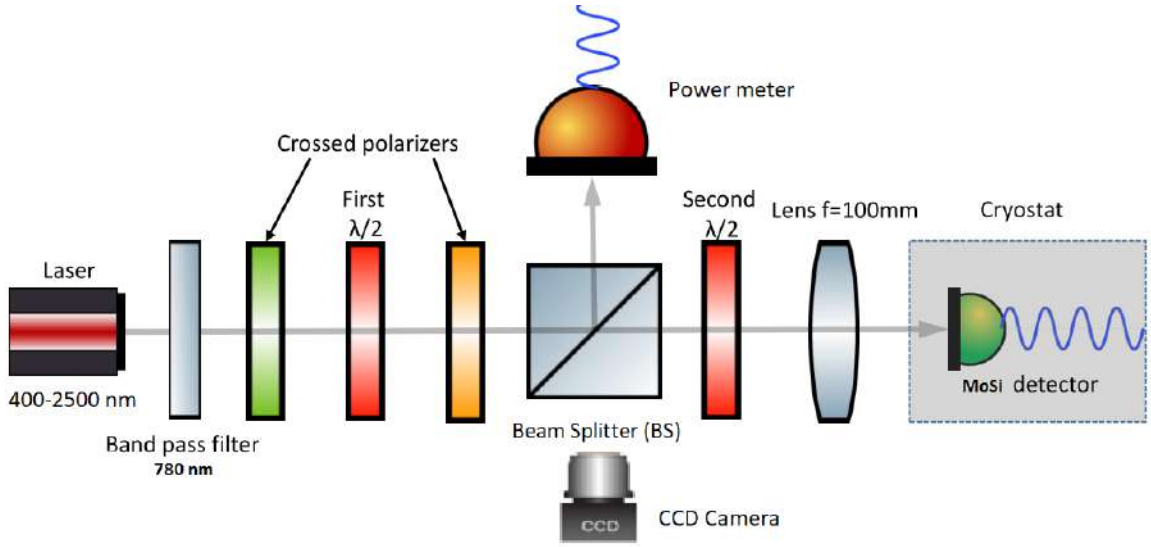

Figure 2.3: Schematic drawing of the optical setup used to perform Quantum Detector Tomography on our SNSPD inside the cryostat

2.2 shows a schematic representation of the optical setup, where some mirrors and filters are elapsed. Our setup starts with a Fianium SC400 pulsed white light laser. This laser source operates at a repetition rate of 20 MHz and creates pulses of 20-30 ps duration. We filter the output of the source with various dichroic mirrors, low-pass filters and a bandpass filter centered around the desired wavelength (780 nm). On the optical table, the laser passes through a crossed polarizer system with a $\lambda/2$ plate between them.This acts as a variable attenuator, allowing to tune the input pump power. By rotating this $\lambda/2$ plate, we vary the transmission according to Malus'law.

$$I(\theta) = I_0 \cos^2(2\theta) \tag{1}$$

where θ is the angle of the $\lambda/2$ plate. It is important to align the polarizers in a perfectly crossed configuration, so the transmission after the attenuator is initially zero. The laser beam must also incide perpendicular to the polarizers, in order to achieve maximum tuning range of the power. Thereafter, the laser beam is directed into the cryostat and towards the detector, passing through various apertures and mirrors. Using the apertures we can calibrate the optical setup, making sure the ray is being directed correctly.

Before illuminating the detector the laser beam passes through a beam splitter (BS), which creates secondary rays that we will use to monitor the power and obtain an image of the laser spot on the SNSPD. A secondary ray is collected with a power meter (Thorlabs PM100D). This ray will allow to estimate the optical power on the detector without blocking the laser beam, using the reflection and transmission coefficientes $(T(\lambda), R(\lambda))$ of the

BS for the selected wavelenghts (780 nm).

On the other arm of the BS, we have a 2x magnification CCD Camera collecting light that comes from inside the cryostat and reaches the camera after reflecting off the beam splitter. This secondary ray, along with a conventional lamp that illuminates inside the cryostat, can be used to image our detector along with the laser beam in real time. The image helps aligning the input laser in order to achieve high count rates. The $\lambda/2$ plate before the window of the cryostat is used to control the polarization of the incoming light, while a lens ($f = 10\ cm$) focuses the laser beam on the nanoconstriction of the detector. In the experiments, the polarization will not be changed so the angle of the $\lambda/2$ plate is kept in the configuration that maximizes efficiency (with the electrical field parallel to the nanowire). The cryostat keeps the SNSPD at a pressure of $\backsim\ 10^{-7}$ mbar, with a base temperature of $\backsim 3.5$ K.

2.3 Electrical circuit

The purpose of the electrical circuit behind the detector is multiple. First, a DC current source must be used to bias the nanodetector close to its critical current. Then, the circuit must also read out and amplify the voltage pulses generated by photon detection.

Let's start with the equivalent circuit for the nanodetector. The detector is modelled by a switch in parallel with a resistor, of value R_N. In series with this, there is an inductor representing the kinetic inductance. This equivalent circuit is represented on the left side of Figure 2.4, and is biased with current I_b. To provide this DC current to the nanodetector, we use a voltage source (Yokogawa GS200) in series with a resistor $R_b = 100\ \Omega$. When the detector is superconducting, the switch is closed and the current I_b flows, set by the voltage source and the load resistor. When a photon incides on the nanowire the superconducting state is destroyed, and the switch opens. This generates a voltage peak that needs to be amplified, and consitutes a 'detection event'. The current now sees a big resistance R_N, of the order of MΩs, so it is quickly shunted into the load resistor due to $R_N >> R_b = 100\ \Omega$. The circuit has now turned into a voltage bias and the cooling of the cryostat can restore the superconducting state of the nanowire. The current I_b will restart flowing through the detector once it is cooled down sufficiently. There is another inductor and a capacitor inside a Bias Tee, which filter high frequencies from the current bias before it enters the superconducting single photon detector. This Bias Tee (ZNBT-60-1W) has a 2.5-6000 MHz bandwidth, and acts as a low-pass filter for the current source.

The second part of this circuit is the readout, amplifying the signal and sending it to an appropiate instrument. To filter out low frequencies from the signal, an extra capacitor is place inside the Bias Tee. We then use a 50 Ω resistance between points A'and B'to match the impedance of the amplifiers with the rest of the circuit. Therefore, reflections of the signal at this point are avoided. The signal of the transient is transferred and it is high-pass filtered by the combination of the capacitor inside the Bias Tee, the 50 Ω resistance

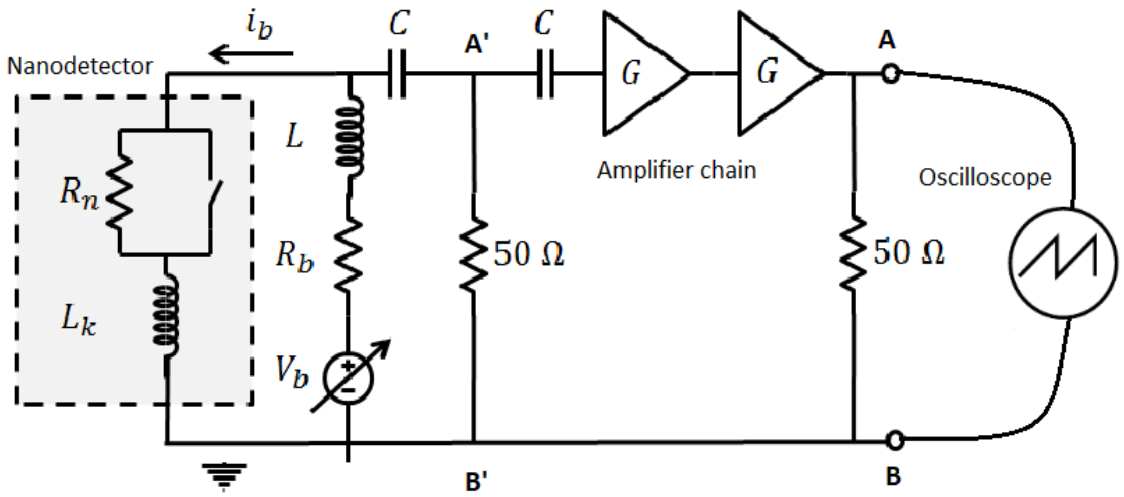

Figure 2.4: Equivalent electrical circuit for the experiment. The shaded area on the left represents the equivalent circuit of the superconducting single photon detector.

and the capacitance at the input of the amplifiers. Only high frequency signals (20-3000 MHz). This voltage is then fed to a set of two RF amplifiers (mini-circuits ZX60-3018G-S+), which are connected to an oscilloscope via coaxial cable. Usually, the oscilloscope is substituted by a pulse-counter (Agilent 53131A) in which we set a trigger voltage to discriminate noise. A typical detection event has peak height of around 0.5 mV. Note that the peak height of the pulse is set by the load resistance R_b and the bias current used I_b. For very low bias currents, detection events can not be recorded reliably, due to a peak height comparable to the background noise.

As mentioned before, resetting the detector is key for this circuit. After photon detection, the switch will be opened due to a resistive barrier happening in the nanowire. This can be seen as a self-heating hotspot where superconductivity is destroyed. The current is directed away from this resistance, on a timescale τ_{fall},

$$\tau_{fall} = \frac{L_K}{R_b + R_N} \tag{2}$$

where L_K is the kinetic inductance of the nanodetector. At the same time, the cooling power of the cryostat will restore the superconducting state of the nanowire. The timescale $\tau_{thermal}$ represents the counteraction between the thermal diffusion of the resistive area and the cooling power of the cryostat. When the nanowire is again superconducting, the current will promptly flow back through the nanodetector.

The timescale for the current returning is τ_{rise},

$$\tau_{rise} = \frac{L_K}{R_b} \tag{3}$$

The kinetic inductance is an intrinsic effect which counteracts rapid changes in the current. It arises from the inertia of high mobility carriers (electrons) in AC current [30]. These carriers have a non-zero mass and need to be accelerated. In alternating fields, an effect analogous to a series inductance appears. The kinetic inductance sets the resetting timescales for this circuit. Therefore, it also sets the maximum count rate than can be achieved. An extensive study on the appearance and role of kinetic inductance in SNSPD's is presented in Ref. [29]. Figure 2.5 shows a typical detection event, from which the reset time can be estimated.

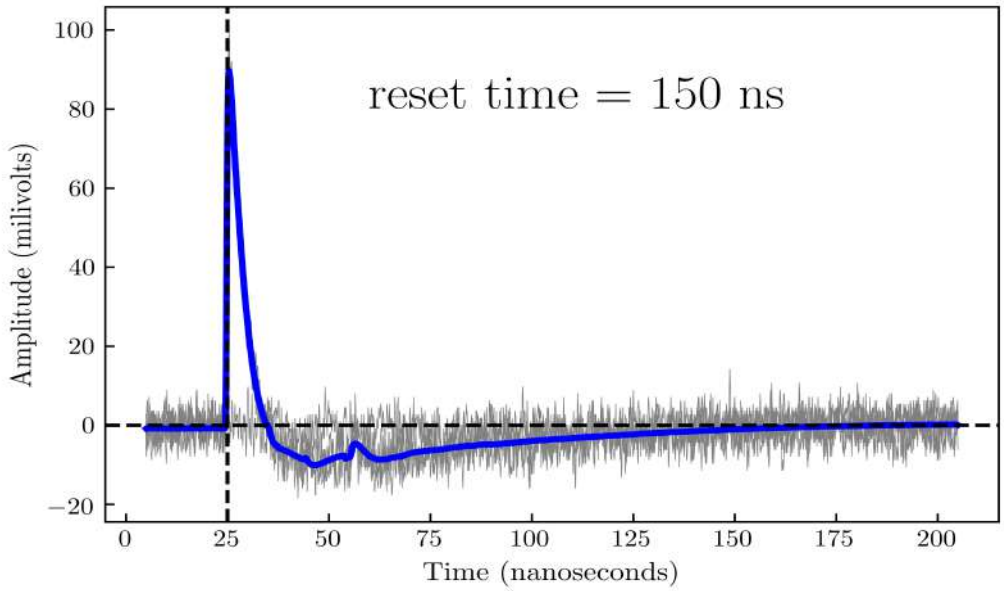

Figure 2.5: Shape of a detection pulse, averaged over 1000 events. The gray trace shows an individual event

Ideally, L_K should be small in order to obtain fast reset times. In practice we cannot have $\tau_{rise} \lesssim \tau_{thermal}$, where $\tau_{thermal}$ accounts for the interaction between the cooling power of the cryostat and the intrinsic Joule heating of a detection event. If the current is restored before the device has cooled down sufficiently, the superconducting state will not be recovered after a detection. The detector will either remain in its normal state or switch between

the superconducting and normal states indefinitely. This is known as 'latching' of the detector, and does not allow any further photon counting [31]. To avoid this, two meanders were added above and under the nanodetector (see Figure 2.2), in order to increase L_K to an acceptable value and avoid latching. From the experimental reset time, we estimate the kinetic inductance to be $L_K \approx 300$ nH. The two meanders also account for most of the resistance of the detector in its normal state R_N.

2.4 Quantum Detector Tomography (QDT)

The main tool we will use to characterize our detector is Quantum Detector Tomography (QDT) [32, 33]. This is an agnostic non-projective measurement method, in which we feed the detector with different coherent states by attenuation of the laser illumination, and measure its count rate. The goal is obtaining the click probability of the detector when N photons are incident on it. We probe the detector with a set of coherent states $|\alpha\rangle$, controlling the input power and then we extract the response of the detector to the photon number states $|i\rangle$. This is achieved by relating the coherent state basis $|\alpha\rangle$ and the photon number (Fock) basis $|i\rangle$. Mathematically, Quantum Detector Tomography is an inverse statistical problem. It is based on the Positive-Operator Valued Measure (POVM) formalism and the problem can be seen as solving this equation for the matrix Π, which contains the intrinsic response of the detector [34],

$$P = F\Pi \tag{4}$$

where P represents the measured statistics and F is the translation matrix between the basis of coherent and Fock states (photon number basis).

The matrix Π is diagonal in the Fock state basis for phase-insensitive detectors, such as this MoSi single photon detector. The diagonal elements of the matrix represent the response of the detector to states with different mean number of photons. These diagonal elements can be written as

$$\pi_n = \sum_{k=0}^{\infty} p_k^{(n)} |k\rangle\langle k| \tag{5}$$

where the coefficients $p_k^{(n)}$ give the weight of each Fock state in the response of the detector. The click probabilities per pulse p_i, given an input coheren state ρ, are defined as $p_{\rho,n} = Tr(\rho\pi_n)$. Therefore, estimating this matrix Π would unveil the complete response of the detector. The two representations, coherent states basis and Fock states basis, are connected through the expression for an arbitrary coherent state in the photon number basis, given by:

$$|\alpha\rangle = e^{-\frac{1}{2}|\alpha|^2} \sum_{n=0}^{\infty} \frac{\alpha^n}{\sqrt{n!}} |n\rangle \tag{6}$$

This poissonian distribution is shown in Figure 2.6.

The goal of Quantum Detector Tomography is obtaining the detection probability of the detector p_i for each state in the Fock basis, which have a well defined mean number of photons i. The method can find this response fitting the experimental data to this tomographic function

$$R_{click}(N) = 1 - e^{-\eta N} \sum_{i=0}^{m} (1 - p_i) \frac{(\eta N)^i}{i!} \tag{7}$$

where $R_{click}(N)$ represents the click probability of the detector for N photons inciding, p_i represents the detection efficiency for i photons and η is a parameter modelling all sources of attenuation. Therefore, QDT can find the response of the detector in the Fock basis $|n\rangle$ by using coherent states $|\alpha\rangle$ as a probe and fitting the results to Equation 7. An important property of coherent states is that they remain coherent after attenuation, lowering the mean number of photons N present in a laser pulse. To simplify the fitting procedure of QDT, a modification is introduced in the technique. Low efficiency detectors, such as this MoSi nanodetector, require many parameters p_i to accurately describe its complete response (at least $\frac{1}{\eta}$ parameters). Introducing the parameter η, which represents all sources of photon loss, tomography now works with the number of photons that are absorbed by the nanodetector ηN, instead of the mean number of photons in the laser pulse N. This method has been previously implemented in Refs. [35, 36, 37], dramatically reducing the number of fit parameters p_i needed to reconstruct the click probability for the detector R_{click}.

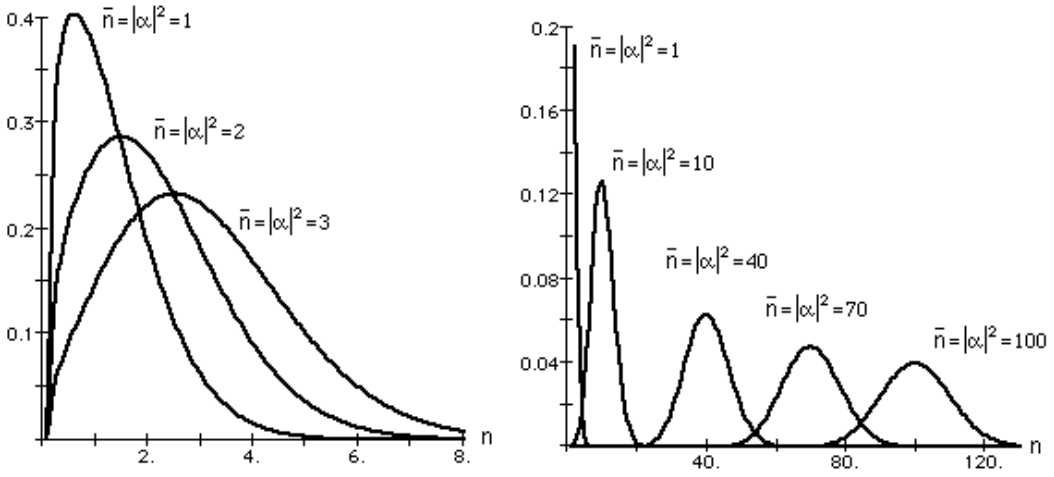

Figure 2.6: Poissonian distribution of the coherent states in terms of the photon number states. The vertical axis representes frequency and the horizontal axis contains the photon number states.

The parameter η represents all losses due to attenuation, alignment and intrisic absorption of the elements in the system. We assume these losses to be linear, differently than the nonlinear multi-photon detection events. Therefore, the experiment is modelled as an attenuated input laser inciding on an ideal (100 % efficient) detector. Experimentally, we feed the detector with attenuated coherent states and then measure the optical power inciding on the detector and the count rate recorded by the detector. The quantities used in the tomographic function are the mean number of photons of the pulse N_i and the normalized click probability for a probe state. To convert measured optical power P_i to mean number of photons per pulse N_i, we use $N_i = \frac{P_i \lambda}{\Omega h c}$, where $\frac{hc}{\lambda}$ is the energy of each photon, and Ω is the repetition rate of the laser. The click probability is equal to the count rate R_i normalized to the laser repetition rate Ω after correcting for the dark counts D_i, $r_i = \frac{R_i - D_i}{\Omega}$. A more detailed look on this tomographic protocol is presented in the Appendix. In Section 3.3.2, we describe how the experimental setup was modified to improve the accuracy of tomography experiments.

3. Resultados experimentales y discusión

En esta sección se presentan los resultados experimentales obtenidos durante el proyecto. Primero, se caracterizan las propiedades superconductoras de este detector de fotón único, encontrando una temperatura crítica superconductora de $T_c = 4.98\ K$. También se analizan las curvas I-V del detector, identificando las regiones que aparece en ellas; y finalmente ajustamos los datos experimentales a una expresión para la corriente crítica proporcionada por la teoría Ginzburg-Landau de la superconductividad. Obtenemos así un valor para la corriente crítica a temperatura 0 K de $I_0 = 30.91\ \mu A$.

En el siguiente apartado, se muestra el ritmo de cuentas (o detecciones de fotón) de nuestro detector de MoSi al variar la corriente a través de él. Comparamos estos resultados con un detector muy similar de NbN, y también se contrastan los resultados con otro trabajo sobre un detector de fotones fabricado en MoSi. A continuación, estudiamos el ritmo de cuentas como función de la potencia óptica que incide en el nanodetector, controlando esta magnitud a través del atenuador variable presentado en el montaje óptico. Este experimento proporciona los datos necesarios para realizar tomografía en este detector, y así obtener su respuesta intrínseca. Se discute la bondad de los resultados, así como previas aplicaciones de la tomografía cuántica sobre detectores de fotón único.

Por último, se muestran dos mejoras implementadas en el montaje experimental con el fin de obtener resultados más precisos en el análisis tomográfico. Se demuestra la conveniencia de introducir estos cambios, realizando medidas experimentales tras su implementación.

3 Experimental results and discussion

3.1 Superconducting characterization of the MoSi SNSPD

3.1.1 Resistance vs. temperature

Let's start by probing the superconducting properties of this nanodetector. We expect the the resistance of the device to decrease rapidly after reaching a critical superconducting temperature T_c. In Figure 3.1, the superconducting behaviour of the nanodetector can be observed. The inset of the figure shows a short circuit used to monitor the resistance of our 150 nm wide detector. The resistance is measured using a $0.7\ \mu A$ probe current while the cryostat is cooled down to base temperature, in order to obtain the resistance as a function of temperature. We find a critical superconducting temperature of $T_c = 4.98K$. This value will be used later to obtain the critical current at 0 K for this detector. For NbN and other crystalline materials, the resistance R increases with decreasing temperatures approaching its critical value T_c [38]. A plausible explanation arises from the crystalline structure of the compound. In a grain boundary scattering models, electrons use thermal energy to hop over these grain boundaries that act as trapping potentials [39].

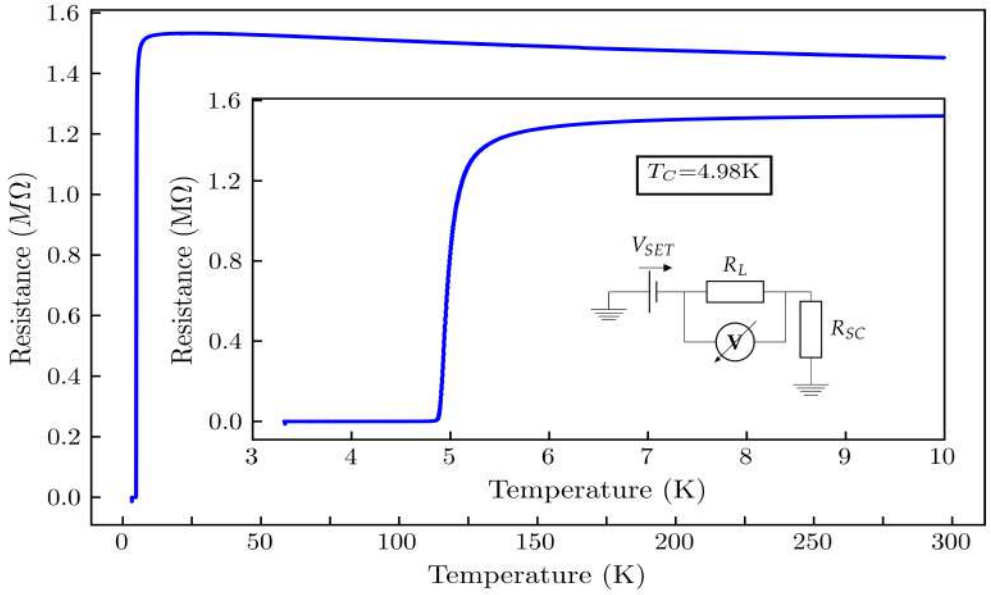

Figure 3.1: Resistance as a function of temperature for a 150 nm wide MoSi constriction, showing that $\frac{d\rho(T)}{dT} < 0$. The inset shows a closer look at the superconducting transition and a schematic picture of the short circuit used to measure the resistance.

Nevertheless, we find similar phenomena for MoSi, which is an amorphous material. Therefore, this explanation for the increase of resistance when lowering the temperature is not satisfactory, as an amorphous material does not contain periodic grain boundaries. Instead, we note that this experimental observations are consistent with the Mooij empirical rule [40]. It states that materials whose resistivity is above 150 $\mu\Omega/cm$ present a negative temperature dependence on the resistivity $\frac{d\rho(T)}{dT} < 0$. In our detector, this value is $\rho = 195$ $\mu\Omega/cm$. Several theories have explored this behaviour observed by Mooij in 1973 [40]. One of these models is that of 'weak localization of the electrons'. In materials with high structural disorder in their lattice, the quantum wavefunction of electrons decays strongly at large distances from the center of the wavepacket. All the relevant states (those near the Fermi energy E_F) are localized, causing electrons to have very low mobility and making the material behave as an insulator. This is common in superconductivity as many superconductors, including all the high T_c superconductors, present a metal-insulator transition at very low temperatures. A rigorous analysis of this phenomena is presented in Ref [41].

3.1.2 I-V curves

I-V curves are one of the main methods to characterize electronic devices. For superconducting devices, one expects a finite amount of current to flow even when the voltage over the device is zero. It is important to note that our circuit is not designed as a pure voltage bias or current bias. Its goal is to restore the superconducting state in the nanowire after detecting a photon, resetting the detector. Consequently, the I-V curves presented here are not strictly standard I-V curves, widely used for the characterization of electric devices such as diodes or junctions.

Figure 3.2 shows an I-V curve for the 210 nm wide MoSi detector, at three different temperatures. Three distinct regimes can be identified: i)The superconducting regime, ii) the breaking of superconductivity and iii) the normal state. We determine the critical current I_c from the limits of the superconducting region, as a sharp transition in the measured current. When the temperature is increased, the superconducting region is reduced and the transition becomes smoother. Note that we are using a voltage source in series with a resistance R_b to feed current to the detector. Therefore, a vertical line indicating zero resistance will not appear for the superconducting state of the detector, due to this load resistance R_b.

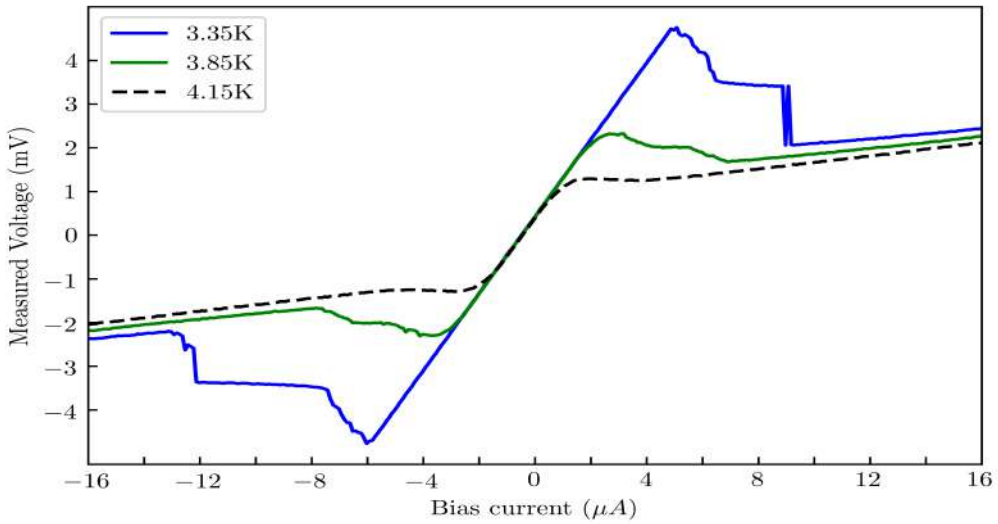

Figure 3.2: I-V curves of the 210 nm wide MoSi nanodetector at different temperatures

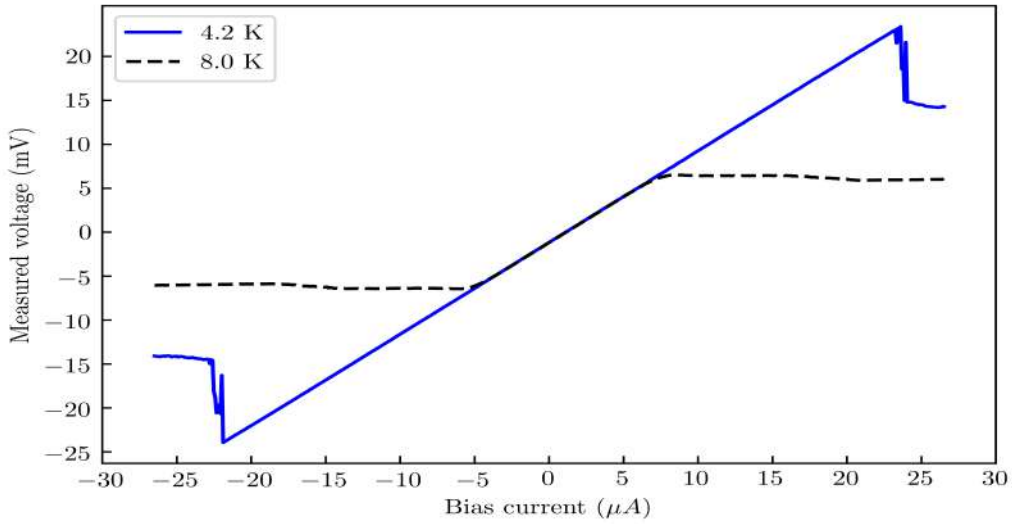

Figure 3.3: I-V curves of the 150 nm wide NbN detector at two different temperatures.

Between $\pm I_c$ the nanodetector is superconducting and presents zero resistance. An ohmic behaviour is observed which we can fit to obtain a total resistance $R_b = 107\ \Omega$. This value represents the load resistance ($\sim 100\ \Omega$) plus some resistance from the wiring in the setup. According to the equivalent circuit for the nanodetector (See Figure 2.3), the switch is closed and the detector has no resistance $R_{SC} = 0$.

When the current reaches I_c, the wire enters a relaxation oscillation regime, in which the detector switches rapidly between the normal and superconducting state. The measured values in this region are not representative, as only a time average of these fluctuations is recorded. The fluctuations happen at a higher frequency than the frequency of the amplifiers used. More information on the relaxation-oscillation regime for these detectors can be found in Ref.[28].

Lastly, when some parts of the detector have become resistive, an ohmic regime with a much larger resistance appears. For currents $-I_c > I > I_c$ we observe linear behaviour with a resistance of the order of $K\Omega s$. If the current was further increased, all parts of the detector would become resistive and we would get back $R = R_N + R_b$. This would be the case of a horizontal line, with slope close to zero. For comparison, we show in Figure 3.3 the I-V curves obtained for the NbN nanodetector at two different temperatures. The curves shown in Figures 3.2 and 3.3 are very similar. NbN shows a bigger superconducting region, as this material has higher values for both critical current I_c and critical temperature.T_c. In both materials, the breaking of superconductivity is less sharp when the temperature approaches its critical value, due to thermal excitations. This makes the detectors less efficient when operating close to their critical temperature T_c.

3.1.3 Critical current vs. temperature

After recording many I-V curves at different temperatures, we extract from them values for the critical current and construct a relation between I_c and T. The criteria for the critical current will be the start of the relaxation-oscillation regime. The last points in this graph have a bigger uncertainty associated, as finding I_c is harder when the transition is less clear for higher temperatures. In Figure 3.4, the decrease of the critical current with increasing temperatures is observed. This can be intuitively understood as thermal excitations contributing to the breaking of superconductivity at lower currents.

Then we fit our values to the expression shown in the graph, from Ginzburg-Landau theory of superconductivity. The fitting provides values for the critical temperature (with zero current applied) and critical current (at T = 0 K) of the detector. It is important to note that I_c will determine the maximum bias current we can use to count photons, and consequently, the maximum pulse height of a detection event. When operating the detector at 3.85 K, the critical current is approximately $2.6\ \mu A$. Multiplying this current by the 50 Ω resistor in the amplifiers and the gain of the amplifier chain, we obtain a pulse height of under 200 mV. This constitutes a problem as now the signal and the noise are comparable,

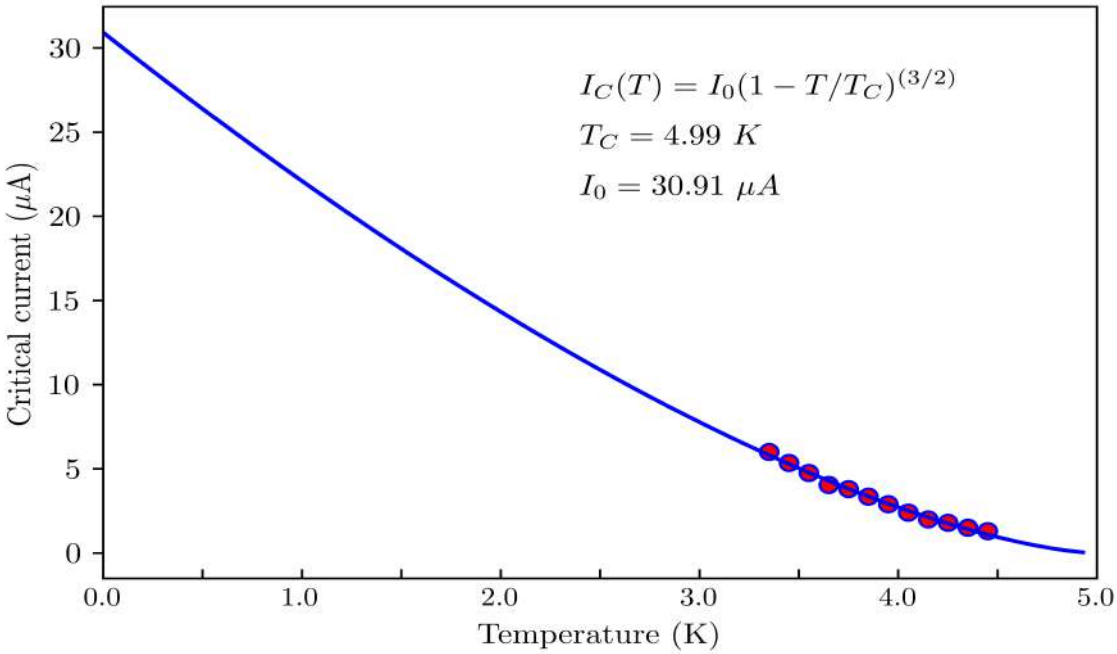

Figure 3.4: Decrease of the critical current for increasing temperatures. Fit was made using the Ginzburg-Landau dependence specified in the graph. Values for T_c and I_0 obtained from the fit are also shown.

and we cannot set a proper trigger voltage. This was experimentally found, as there were no significant counts above $T = 3.85\ K$. This problem can be solved by using amplifiers with less noise, operating at lower temperature or including a low pass filter to eliminate the low-frequency noise.

3.2 Photon counting properties

3.2.1 Detection efficiency of the nanowire

So far, we have only characterized the material and conducting properties of the detector. Let's now look into the detection events (or counts) that the detector records. In SNSPD's, a detection event occurs when the arrival of one or more photons affects the superconducting state of the wire, driving it to the resistive state temporarily and creating a voltage pulse.

To characterize the detector, we record its count rate, the current flowing through it and the optical power inciding on the detector. Before presenting the experimental results, let's outline the features of these detectors that will not be experimentally probed. In this thesis, we will not consider the Local Detection Efficiency [42] which is the profile of efficiency

of the nanowire along its width. In short, the edges of the detector are more sensitive to detecting photons, since they have a lower threshold current for photons for a fixed energy. If we increase the bias current I_b, the efficiency will increase throughout the wire but it will remain higher for photons absorbed near the edges of the nanowire. [43].

In addition, the detection efficiency of this device depends on polarization. When illuminating the single photon detector with light polarized parallel to the length of the wire, the count rate will be higher than for any other polarization. This polarization dependence is due to the boundary conditions that appear when solving Maxwell's equations for the light inciding on the detector. Furthermore, we can play with the width of the nanowire to test this effect. Narrower wires will have a higher efficiency overall (because there's more 'edge'), but a lower ratio between polarizations $\frac{R_{\parallel}}{R_{\perp}}$ because of the loss in efficiency detecting perpendicularly polarized light. Lastly, optical cavities have been demostrated to enhance the efficiency of the detectors[44]. It seems likely that any future application of this technology will be paired with a proper optical cavity, in order to obtain a better performance.

3.2.2 Counting photons

In this section, we will study how the count rate of our detector changes when the bias current is modified. If the detector is biased close to its critical current $I_b \approx I_c$, the energy of a single photon will be enough to break superconductivity and produce a count. In this situation, most pulses from the laser will trigger a detection event, as these pulses contain millions photons at minimum. Therefore, the count rate is expected to approach the laser repetition rate, i.e. the number of pulses per second produced by the laser. This value is 20 MHz for our pulsed laser source.

Conversely, as the bias current I_b is lowered, we expect the count rate to decrease, given that now the device is further from the superconducting-to-normal transition and it may require more than one photon to trigger a detection. This multi-photon events are less probable, as the two photons must be absorbed very close in both space and time. As discussed earlier, the nanowire geometry of our detector restricts the area where photon detection happens, improving the chances of recording multi-photon events. As discussed in Section 3.1.2, once we bias the detector very close to its critical current I_c , we enter the relaxation-oscillation regime where we can no longer extract meaningful information from the count rate. In fact, count rates higher than 20 MHz can be recorded in this regime, in which the nanoconstriction oscillates between the normal and superconducting state.

In this experiment,the total count rate is recorded, including photon counts and dark counts. By repeating this measurement while blocking the laser beam, we can extract the rate of dark counts and substract it from the total count rate. The voltage pulse created by a dark count is identical to that of a photon detection. Nevertheless, dark counts have an exponential dependence on bias current, which also helps distinguishing photon and dark

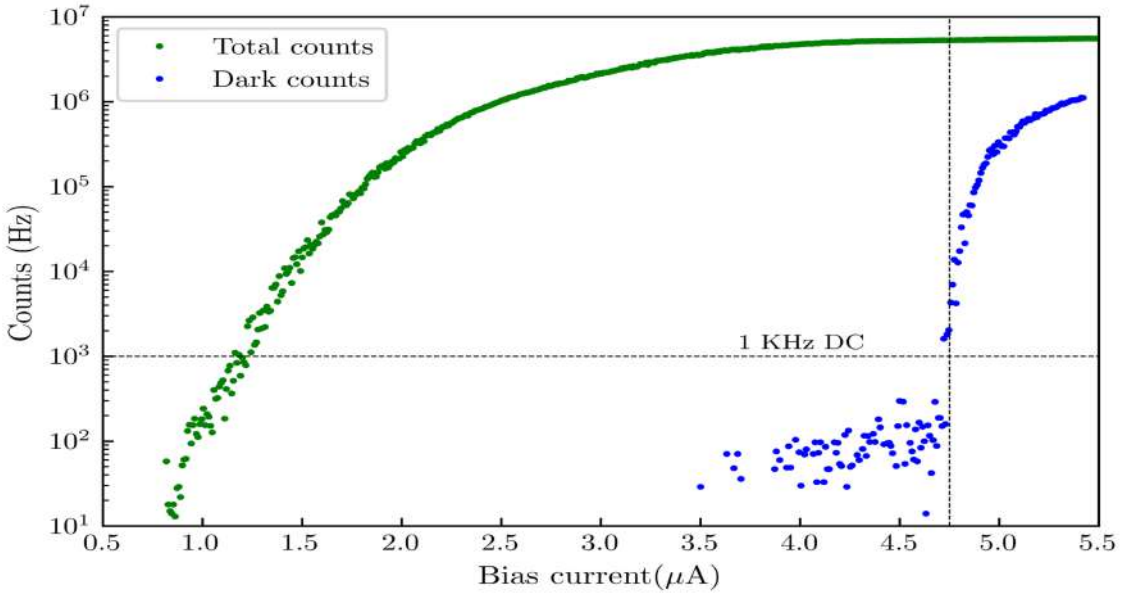

Figure 3.5: Count rate of the MoSi detector when approaching its critical current, $I_c = 6\ \mu A$. The used wavelength is λ = 780 nm. Dashed lines indicate current for 1 KHz of dark counts

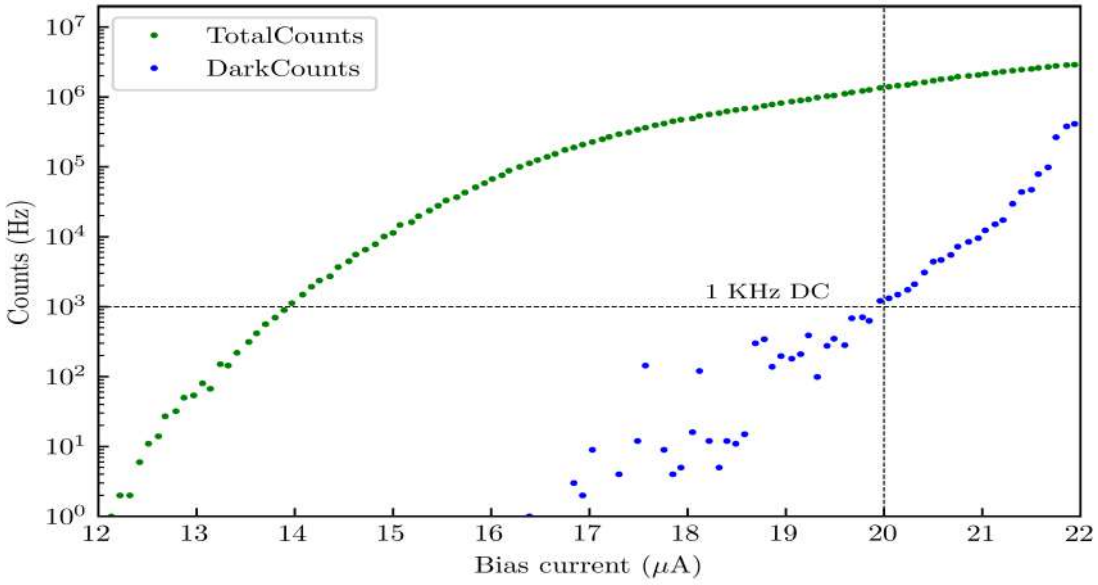

Figure 3.6: Count rate of the NbN detector when approaching its critical current, $I_c = 22\ \mu A$. The used wavelength is λ = 780 nm. Dashed lines indicate current for 1 KHz of dark counts

counts. In literature, there's a consensus about dark counts being due to thermally activated vortices crossing the wire[26, 28, 21, 45]. The movement of the vortices dissipates energy which breaks the superconducting regime [46]. It has been shown that dark counts increase significantly if the temperature is increased or if a magnetic field perpendicular to the wire is applied. [47].

In Figure 3.5 and 3.6, we show the count rate for our MoSi and NbN detectors when illuminated with 780 nm laser light. Both measurements were performed at base temperature $T = 3.35\ K$. The maximum count rate achieved in the MoSi nanodetector is 6 MHz, slightly lower than the count rate of the NbN nanodetector. The count rate of both single photon detectors is similar when increasing the bias current towards its critical value I_c. As expected, the count rate in the MoSi nanodetector is highest for currents near the critical current, as just one photon is enough to break superconductivity in this scenario. Dark counts are also higher when close to the critical current, but they always remain significantly lower than photon counts.

One main difference is the range of bias currents. For MoSi, this interval is much smaller than for NbN, due to the lower critical temperature T_c in MoSi. This means that the base temperature of our cryostat ($T_c = 3.35\ K$) is closer to T_c for this material, and the critical current is significantly reduced (See Figure 3.4). As mentioned before in Section 3.1.3, the signal to noise ratio will limit the temperature at which the detector can detect photons consistently. For comparison, in previous studies for this NbN detector, counts were reliable up to a relative temperature of $t_r = \frac{T}{T_c} = 0.88$. On the other hand, using the MoSi nanodetector we could detect photons reliably up to $t_r = 0.79$.

Dark counts also show a different behaviour. The MoSi detector records 1 KHz of dark counts at a current very close to I_c, in contrast to NbN. This may suggest that MoSi has less dark counts overall, making it a prime candidate for quantum information applications. The dark count rate of NbN shows a clearer exponential growth for all current values. Meanwhile, in MoSi dark counts for low bias currents seem to have a random statistical spread. These dark counts start growing exponentially from 4.7 μA onwards, possibly signaling a different cause to these dark counts at low currents.

Lastly, we plot the counting rate of the MoSi nanodetector in a linear scale. The purpose is to compare it to previous results by M. Caloz *et al* [25], where an universal saturation of the count rate is found for various photon wavelenghts. Let's remind what could cause saturation in these detectors. SNSPD's maximum count rate will be limited by either the laser's repetition rate, or the reset time of the electrical circuit (set by the kinetic inductance). From the voltage pulse we estimated the reset time of our detector to be 150 ns, which would give a detector maximum count rate of 6.66 GHz, much bigger than the 20 MHz repetition rate of the pulsed laser. Therefore, this MoSi nanodetector could reach saturation at 20 MHz.

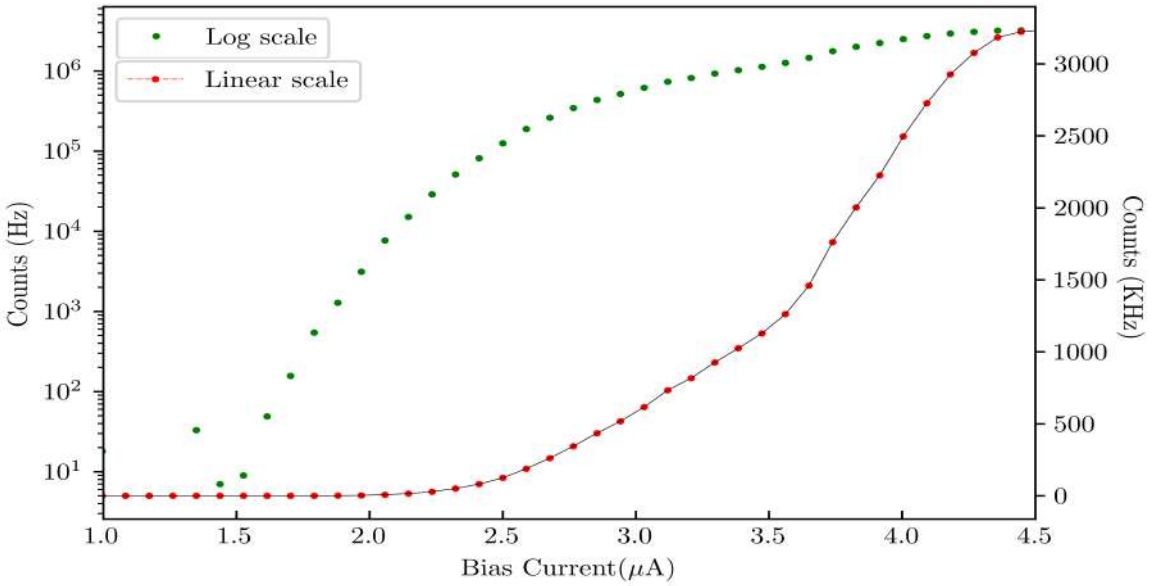

Figure 3.7: Photon count rate of the MoSi detector while increasing the bias current at 3.35 K. The used wavelength is λ = 780 nm. The count rate shows first signs of saturation.

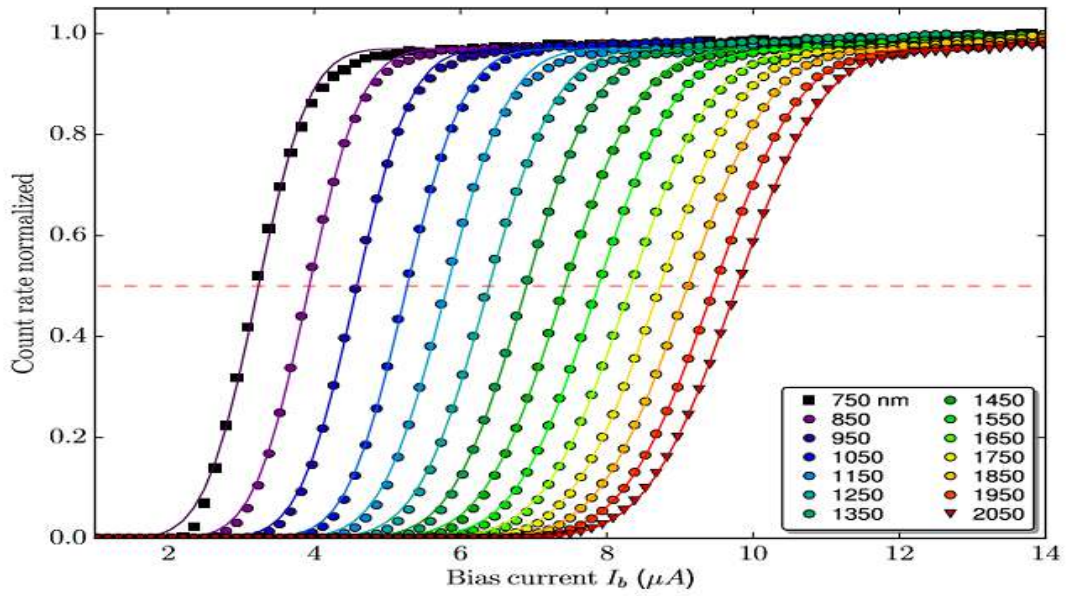

Figure 3.8: Count rate of a MoSi meander when approaching its critical current at T=0.75 K [25]. M. Caloz et al found universal saturation of the count rate for different wavelengths, i.e. photon energies.

In Figure 3.7, the count rate shows first signs of saturation when approaching I_c. This result is not conclusive, as the experiment should be repeated for different wavelengths in order to possibly reproduce the results of Figure 3.8. It's unclear if this saturated count rate is a feature of the material (MoSi being an amorphous superconductor) or the geometry of the detector (meander or nanodetector). This universal saturation has not been found for NbN nanodetectors studied in this experimental setup. Achieving a higher count rate, closer to 20 MHz, is also desirable in order to compare these results to other works on MoSi superconducting single photon detectors.

3.3 Applying tomography to a MoSi nanodetector

3.3.1 Count rate vs. power

The following experimental results constitute the raw data used for the tomographic analysis of the detector. The count rate is recorded while varying the input pump power by attenuation of the laser beam. The bias current remains constant (we choose a point in the horizontal axis of Figure 3.5). The tuning of the power is achieved using the variable attenuator, formed by two crossed polarizers with a $\lambda/2$ plate between them. The rotation of this half wave plate provides the whole range of optical power transmission. Hence, a set of points (R_i, P_i) is obtained for each bias current choice. The results are shown in Figures 3.9 and 3.10 for three different bias currents. Figure 3.9 shows the data on a log scale for the count rate, while Figure 3.10 features a double logarithmic scale. As expected, the count rate is higher when we increase the bias current. For low transmission, the counts grow very fast for all currents. When approaching 100 % transmission, the counts stabilize at different values for each bias current.

Multi-photon events are expected to be prominent for lower bias currents. As demonstrated in Ref [48], if we plot this measurements in a double logarithmic scale, the slope of the curve indicates the dominant i-photon event. A slope equal to one would signal a one-photon regime and a slope equal to two would indicate that two photon events are dominant at this bias current. This is shown in Figure 3.10, where all three bias current choices present linear behaviour with slope $m = 1$. This is different from results obtained in NbN, as higher slopes (at least m=2) are expected when using bias currents far from the critical current. These multi-photon events do appear in the crystalline NbN, but it is still unclear if a two-photon regime exists for this MoSi nanodetector.

In any case, Quantum Detector Tomography would unveil this regime and other features of the detector. For tomography purposes, it is desirable to have very low count rates for low powers and to approach saturation (20 MHz) when the transmission is 100 %.

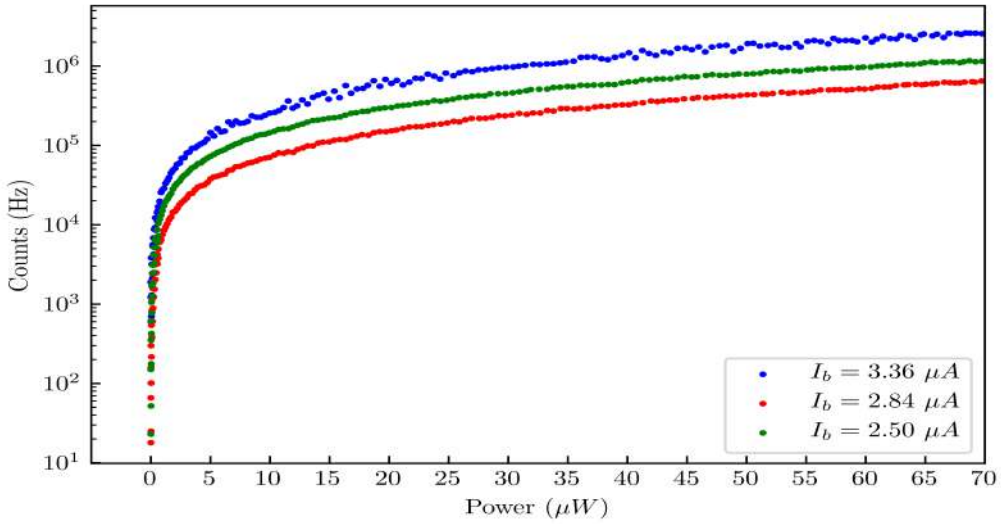

Figure 3.9: Counting rate of the detector as a function of optical input power for three different bias currents, on a logarithmic scale. The power is increased by rotating the $\lambda/2$ plate in our variable attenuator.

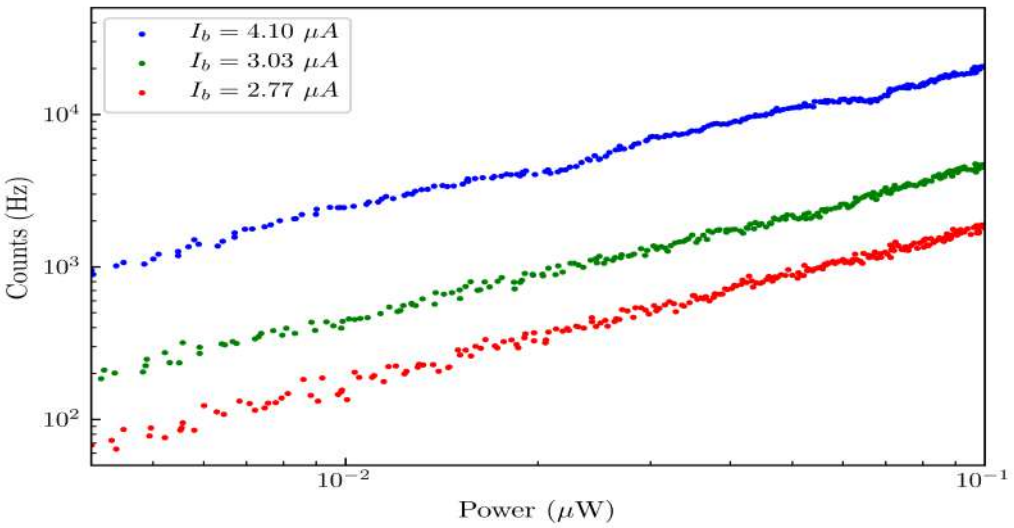

Figure 3.10: Double logarithmic scale plot of the count rate as a function of optical input power. There is a slope equal to one for the three bias currents, signaling one photon regimes.

In order to apply the QDT formalism explained in Section 2.3, the count rate and the incident optical power are recorded. Then, these quantities are transformed into a click probability r_i and a mean number of photones per pulse N_i. Therefore, Quantum Detector Tomography will take datasets of the form (r_i, N_i) and extract extract the probabilities p_i for $i = 1, 2, 3, ...K$ while filtering linear losses using the parameter η. Applying the tomographiy involves fitting the data mentioned above to Equation 3.1:

$$R_{click}(N) = 1 - e^{-\eta N} \sum_{i=0}^{m} (1 - p_i) \frac{(\eta N)^i}{i!} \tag{8}$$

It is very important to separate the notions of absorption efficiency and detection probability. There are many elements in the setup that can induce a loss of photons, i.e. an attenuation of laser light.It's difficult to investigate the response of the detector without separating the external processes. To do so we define a linear parameter η related to an absorption efficiency. In this way, the response of the detector can be analyzedusing the number of photons that actually reach the detector and are absorbed by it. These photons are our candidates for 'light counts'. Using the size of the detector, the optical spot and a $\sim 25\%$ absorption for the NbN film, we have a rough estimate for these linear losses of $\eta = 10^{-5}$.

At the time of elaborating this text, the tomographic fitting had not been sucessful with the experimental data for MoSi. This constitutes the obvious next step to characterize this superconducting single photon nanodetector. Successful tomography measurements require the data from Figure 3.10 to deviate from a straight line, so it's possible to fit multiple parameters, i.e. η and p_1. To illustrate the application of Tomography to a similar detector, 2 graphs from Ref. [26] are presented. These measurements were made on the 150 nm wide NbN nanodetector previously mentioned, which has a 5 nm thickness and an active area of 200x150 nm

Figure 3.11 shows how the parameters p_i and η change with bias current. As mentioned before, at low currents, the energy of a photon may not be enough to break the superconducting state in the constriction. Therefore, multi-photon events represent a significant fraction of the photon detections. As we increase the critical through the nanowire, one-photon detections are now possible and the multi-photon events become much less probable. The parameter η , which represents a linear loss of photons, remains nearly independent of current. This is consistent with our assumption on the attenuation being a linear process. The authors of Ref. [26] estimated $\eta \approx 10^{-4}$ for the NbN nanodetector..

Figure 3.12 shows the total count rate reconstructed from the different photon number regimes. The data corresponds to a low bias current point, where multi-photon events are expected to be significant. It's important to remark that different multi-photon processes become important for different levels of optical power on the detector. This is illustrated

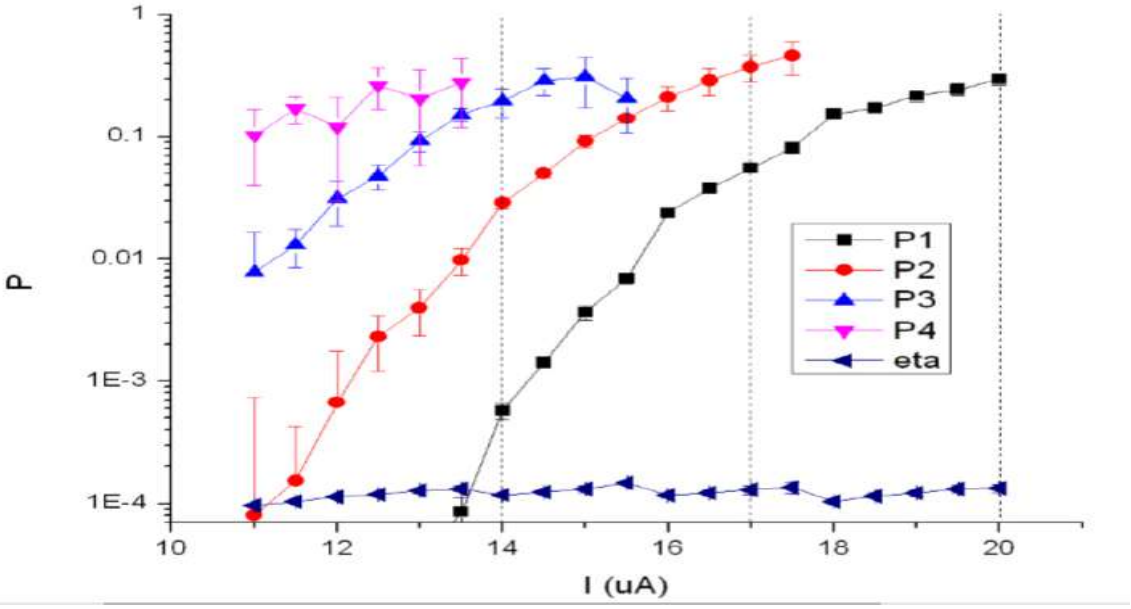

Figure 3.11: Tomography results showing the values of p_1, p_2, p_3, p_4 at different bias currents at a wavelength of 1.5 μm. The parameter η remains nearly constant throughout the current range. Graph from J.J. Renema's PhD thesis [26].

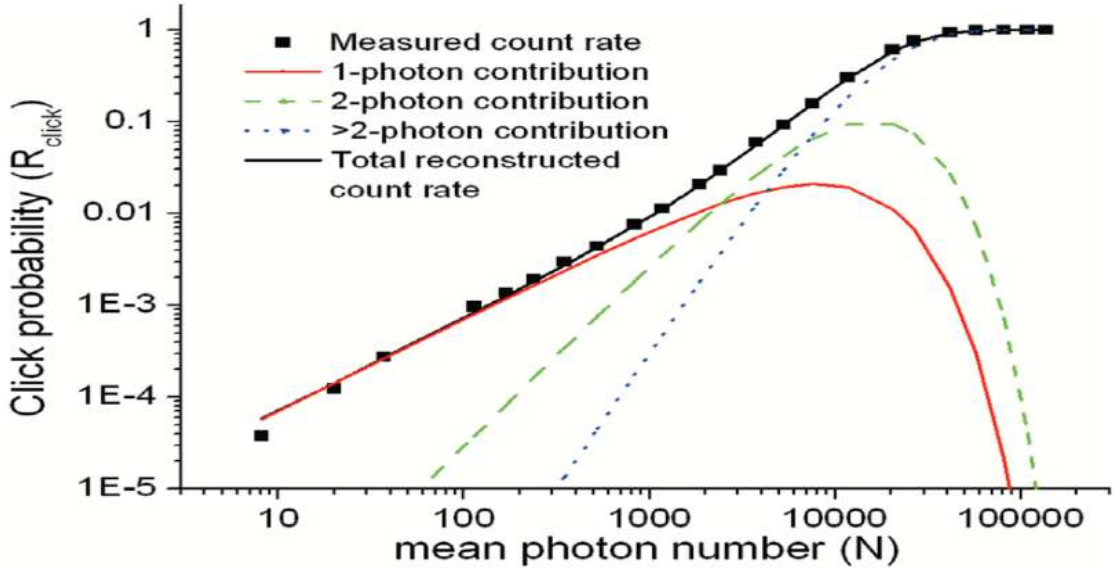

Figure 3.12: Total photon count rate, with separate contributions from different photon regimes. Graph from J.J. Renema's PhD thesis [26].

by the horizontal axis of Figure 3.12, already converted into mean number of photons per pulse. This graphs show the usefulness of Quantum Detector Tomography, as it can separate the various contributions and extract the parameters to characterize the detector in a single experimental run.

3.3.2 Improving tomography experiments

At the initial stage of the research, there were some aspects of the experimental setup that limited the accuracy of the measurements. Consequently, these problems made tomography harder to apply reliably on single photon detectors. Two changes were implemented in the setup to improve its overall performance. Now, these two changes will be presented, along with the reasoning behind the modifications.

As mentioned in the optical setup, when rotating the half wave plate in our variable attenuator, we expect the power and the count rate to follow Malus' law. At an initial stage of this research, the measured count rate did not follow Malus' law correctly. We attributed this deviation to some external fluctuations (in temperature, position of the laser, vibrations) that were noticeable because the spot size of the laser and the amplitude of the deviations were comparable. In other words, these fluctuations were moving the laser beam out of the active area of the detector, causing a drop in the count rate.

Conversely, the power meter recorded a good Malus' law because its active area is much bigger than the laser spot size and the amplitude of the deviations. Therefore, these fluctuations were not significant, as the laser spot was still on the active area of the power meter. In order to solve this, wa beam expander was removed from the setup. The purpose of this element was to enlarge the laser beam before the final lens, so we had a smaller spot size when focusing on the detector, increasing the overall efficiency. Removing the beam expander made the laser spot bigger, making the count rate less sensitive to these fluctuations. The tradeoff is a loss in efficiency, as now more photons are hitting the detector outside of its active area. Figure 3.13 shows the count rate as a function of the angle of the $\lambda/2$ plate at the initial state of the experiment (left) and after removing the beam expander (right).

Another possible improvement of the experiment is to simultaneously monitor the power and the count rate. The beam splitter in our setup allows us to measure the power on the detector in real time, using a secondary ray directed towards a power meter. As stated before, knowing the transmission and reflection coefficients for this beam splitter allows to relate the optical power on the power meter and the optical power on the detector. In previous works using Quantum Detector Tomography [26, 37], the relationship between the angle of the $\lambda/2$ plate and the optical power transmitted towards the detector had been taken at a time t_0. On the other hand, the counting rate for changing angle was measured

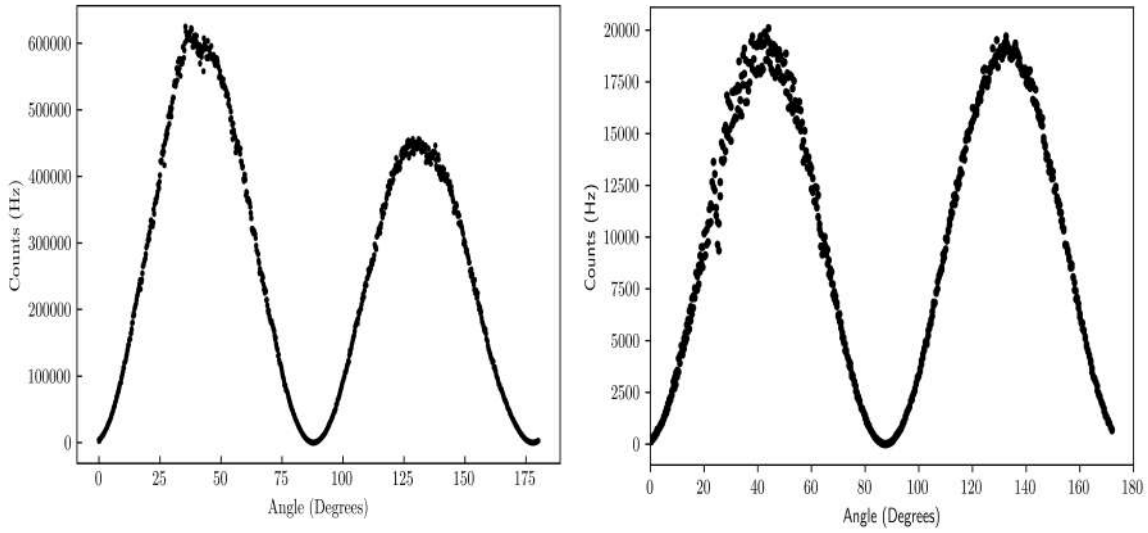

Figure 3.13: Count rate vs. angle before and after removing the beam expander. The bigger spot size on the detector minimizes the effect of other fluctuations, and the data follows Malus' law for the improved setup.

at a different time t_1. The datasets used for tomography were of the form:

$$[R_i(t_1), P(t_0)] \tag{9}$$

This constitutes a problem if the optical power depends on time $P = P(t)$, because we would be assuming the optical power for each angle is precisely the input optical power measured at time t_0. Making use of the beam splitter, we measure both variables at the same time and obtain complete data sets in one run. It's important to note that this is not an improvement by itself. This treatment will only enhance tomography if these two measured magnitudes are correlated: without correlation the data could be replaced by the time average. To verify the correlations we fix the angle, bias current and temperature and let the detector count photons for several hours (14 hours). Figure 3.14 shows the cloud of points obtained.

Applying the Pearson criteria, a moderate linear correlation is found between count rate and optical power, with a value of $\rho = 0.45$. This implies that we can enhance the accuracy of tomography by introducing the complete data sets $[R_i(t), P_i(t)]$, instead of the average $[\bar{R}, \bar{P}]$ as the correlation contains extra information.

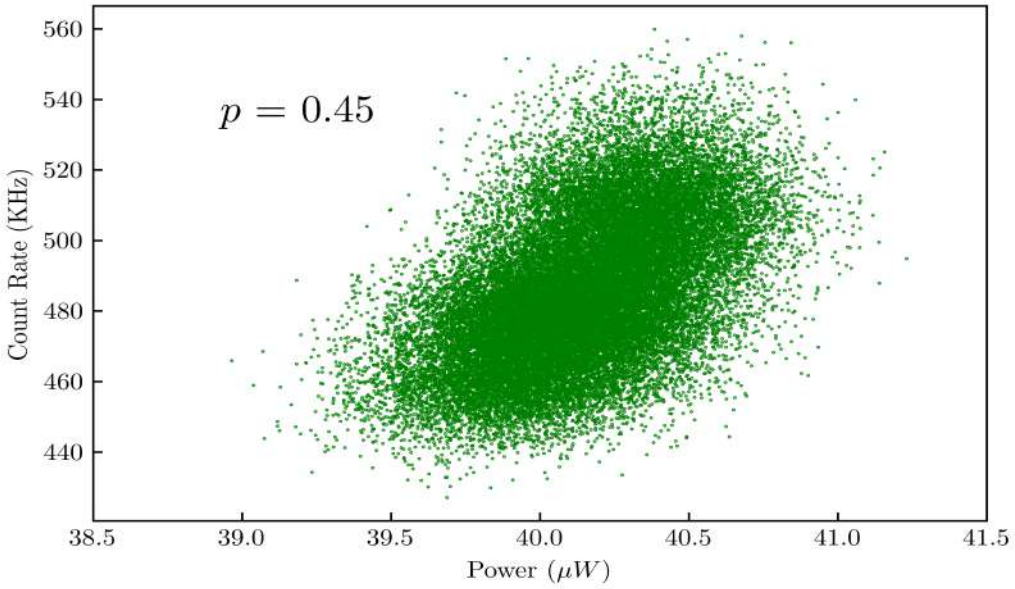

Figure 3.14: Cloud of points for fixed count rate vs. power. We find a moderate linear correlation.

These two changes in the experimental setup have been proven to help the consistency and accuracy of the measurements needed to perform tomography. Both this changes were implemented, and will hopefully allow us to obtain better data sets and record reliable multi-photon events. This would help characterizing the complete response of this MoSi superconducting nanowire single photon detector. Quantum Detector Tomography can unveil the underlying detection mechanism of these devices, a key step towards designing and fabricating better detectors for future applications.

4. Conclusiones

En este trabajo, hemos caracterizado un detector de fotón único de nanocable superconductor, fabricado en MoSi. Hemos demostrado el carácter superconductor del nanodetector, hallando una temperatura crítica superconductora de $T_c = 4.98\ K$ y una corriente crítica superconductora a 0 Kelvin de $I_c(0) = 30.91\ \mu A$. Las curvas características I-V muestran un comportamiento similar al del NbN cristalino, aunque el nanodetector de MoSi posee un rango superconductor más pequeño. En cuanto a su rendimiento detectando fotones, hemos estudiado su ritmo de cuentas en función de la corriente que circula por el nanocable, encontrando diferencias cualitativas con resultados anterior de Caloz *et al*. El máximo ritmo de cuentas obtenido fue de 6 MHz, por debajo del nivel de saturación obtenido con el nanodetector de NbN (20 MHz). Obtener un mayor ritmo de cuentas es deseable a la hora de contrastar estos resultados, así como utilizar un rango amplio de longitudes de onda. La corriente crítica experimental a la temperatura base del sistema fue de $I_c = 6\ \mu A$ con $T = 3.35\ K$.

Hasta ahora, no se han registrado suficientes eventos de más de un fotón, lo cual hace que no sea posible aplicar el método tomográfico al detector usando estos resultados. Se esperaba hallar un régimen donde los eventos multi-fotón fueran dominantes al aplicar una corriente baja. Más investigación es necesaria en esta dirección, con el fin de aplicar la Tomografía Cuántica de Detectores y obtener la respuesta completa del nanodetector de MoSi. Por último, se presentan dos mejoras al montaje experimental. La exclusión de un expansor de haz hace que el sistema sea más robusto frente a fluctaciones (cambios de temperatura, vibraciones), a cambio de una pérdida de eficiencia. Por otra parte, la introducción de divisor de haz genera hasta dos rayos secundarios que utilizamos para obtener una imagen del detector y el láser en tiempo real, así como monitorizar la potencia óptica sobre el detector en todo momento. Se halla una correlación linear entre el ritmo de cuentas y la potencia óptica, justificando que obtener datos simultáneos de estas dos magnitudes mejora la precisión del proceso de ajuste tomográfico.

Obtener una saturación del ritmo de cuentas, así como identificar regiones donde los eventos de multi-fotón sean dominantes, son los siguientes pasos en esta investigación. Esto nos permitirá aplicar eficientemente la técnica tomográfica sobre este nanodetector superconductor de MoSi, obteniendo todos los parámetros η y p_i que caracterizan la respuesta del detector de fotón único.

4 Conclusions

In this thesis, we studied a Superconducting Nanowire Single Photon Detector made out of MoSi, an amorphous superconductor. We characterized the superconducting properties of the 150 nm wide detector, which has a critical superconducting temperature of $T_c = 4.98\ K$. The obtained critical current at 0 Kelvin for this detector is $I_c(0) = 30.91\ \mu A$. The measured I-V curves of the MoSi nanodetector are similar to those of the NbN nanodetector. The latter shows a wider superconducting range, related to the higher critical temperature T_c and critical current I_c of NbN. In both cases, increasing the temperature decreases the superconducting range and makes the transition to the normal state less sharp. For the count rate as a function of bias current, we found qualitative differences with previous results reported by Caloz *et al*, as an universal saturation of the count rate was not found. Still, it is desirable to achieve higher total count rates as well as probing a wider range of wavelengths with this MoSi nanodetector. The critical current at base temperature $T = 3.35\ K$ was $I_c = 6\ \mu A$ and the maximum count rate achieved was 6 MHz, below the expected saturation at 20 MHz. The rate of dark counts appeared to be lower for Mosi than for NbN, as well as presenting a different spread for low bias currents.

So far, multi-photon events have not been recorded reliably, making tomography in the MoSi detector not possible. This was not expected, and further investigation is required to characterize the full response of this single photon detector. Lastly, two improvements were implemented in the setup, in order to enhance tomography. A linear correlation between measured count rate and measured power was found, providing an opportunity to enhance the accuracy of the tomographic routine. Increasing the beam size (at the cost of coupling efficiency) allowed us to counteract external fluctuations such as temperature changes or vibrations. Obtaining a clear saturation of the count rate, as well as observing multi-photon events will allow us to better obtain the values of p_i and η and perform tomography on MoSi. This will characterize the intrinsic response of the detector, a key step in understanding the physycal process behind photon detection with these devices.

5 Appendix

Uncertainty in the measurements, limiting magnitude

In this experiment, we measure different magnitudes such as power, temperature, current,etc... We briefly give values for the relative uncertainty of these measurements, in order to identify which is the main source of error in the setup, and to possibly improve the experiment and enhance the overall accuracy of the data.

Temperature: We expect the temperature values to fluctuate because the vacuum and cooling systems are non-ideal. The variations in temperature are reduced if the system is stabilized at the base temperature (3.35 K):

$$T = 3.35 \pm 0.02\ K \tag{10}$$

amounting to a 0.6 % relative uncertainty in temperature. This data was taken over a 16 hour long measurement, proving that our cryostat and cooling system are stable over time.

Bias Current: The uncertainty in bias current arises from the instrument precision of the voltage source (Yokogawa). Operating this device in the proper range, we have an experimental uncertainty of 10^{-5} mV corresponding to the last digit we can read off this voltage source. We will treat this uncertainty as fluctuations in current (noise) and ignore the uncertainty in the value of the 100 Ω resistor. Therefore, our uncertainty in the bias current through the detector is:

$$I_b = 15\ \mu A \pm 10^{-2}\ \mu A \tag{11}$$

In the cryostat, there's a temperature gradient between the outside environment and the heat shields (3 K and 50 K shields). This introduces a thermal voltage offset, that is considered to be constant for small temperature changes. All our experiments were done in the 3-10 K temperature range. We find this value of thermal voltage offset by looking at the I-V curves and their asimmetry around the point (0,0). The experimental value for this offset is $V_{offset} = 1.21\ mV$.

Optical Power: This laser (and every non-ideal light source) presents some fluctuations in the intensity of the light. We measure this in the statistics mode of our power meter for a moderate power level and a long timescale (14 hours). We expect the power fluctuations to have a gaussian spread around a mean power, as predicted by the theory of coherent states in quantum optics. The shot noise, i.e. minimum standard deviation attainable, is given by $\sqrt{N}$, where N is the number of photons per pulse corresponding to our mean power (40 μW). After applying the transformation from power to mean number of photons per pulse,

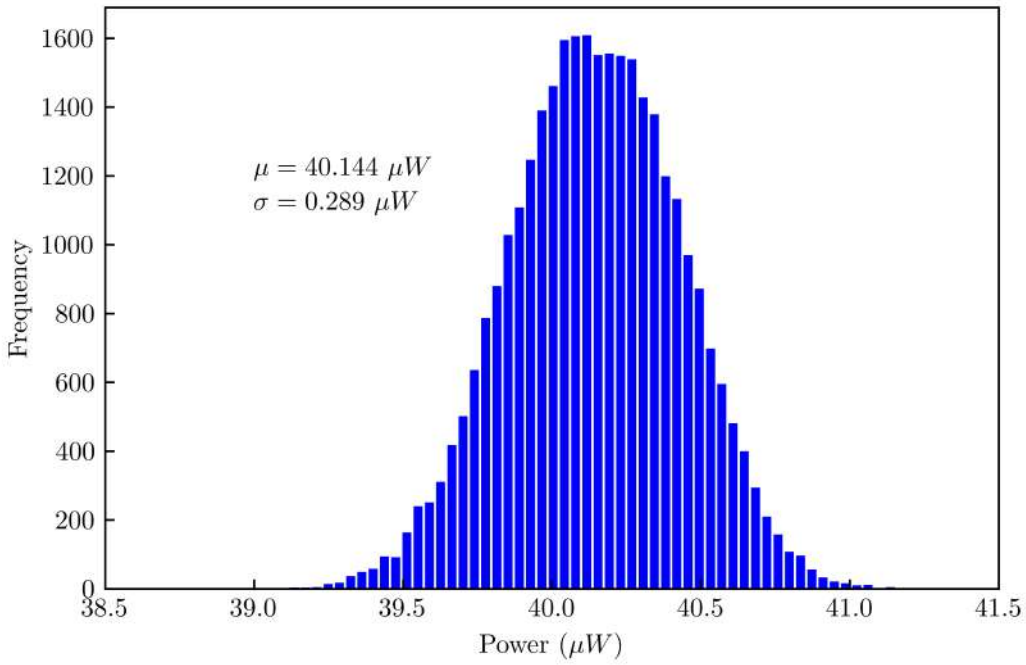

Figure 5.1: Histogram of the power fluctuations in our power meter, showing a gaussian distribution. Data was taken over 14 hours

we obtain a shot noise of σ_{SN} = 14.3 nW. The experimental data presents larger variations, shown in Figure 5.1.

$$P = 40.144 \pm 0.298\ \mu W \tag{12}$$

$$\sigma_P = 20.84\ \sigma_{SN} \tag{13}$$

The relative fluctuations in power were found to be around 0.7 % of the power.

Count Rate: The photon counting process is also of statistical nature. Every time a photon is absorbed by the detector, we can 'roll a dice' to determine if it is detected or not. This process is repeated Ω times per second, where Ω is the repetition rate of the laser. Therefore, the count rate can be modelled as a binomial counting process.

We obtain the error in the count rate fixating the angle (therefore fixating the mean power) and recording the count rate for 10 seconds in each point. In this way we find a relation between the standard deviation in count rate versus bias current shown in Figure 5.2. We can also compute the standard deviation of the count rate versus the mean count rate at each point.

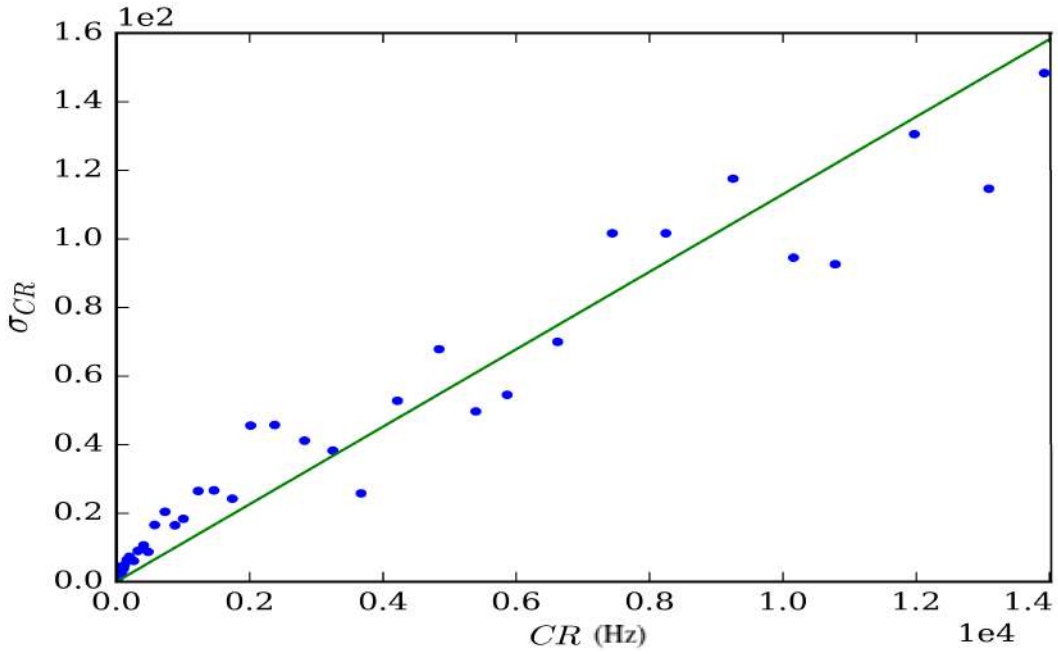

Figure 5.2: Normalized standard deviation of the count rate. The fluctuations were integrated over 10 seconds for each point. Graph provided by E. Abeln.

Instead of a binomial statistical spread, we find a linear increase in the error that is proportional to the count rate. For a binomial process, the uncertainty should decrease for higher count rates. Instead, we observe an uncertainty that increases as we reach higher count rates. This will be helpful to model the error when adding noise to the tomographic code.

$$CR = 6 \text{ MHz} \pm 30 \text{ KHz} = 6 \text{ MHz} \pm 0.5 \ \% \tag{14}$$

The normalized standard deviation (divided by the count rate value), has a constant value around 0.5 % of the count rate. This will help us modelling the error in the count rate, when testing the robustness of our Tomography code.

Model selection in tomography

The procedure can be really demanding when working with a non-ideal detector, so we will use a modified technique introducing η as a linear loss (ratio between input photons and absorbed photons) in the tomographic function depicted below. Grouping linear losses into one parameter , η , will significantly reduce the number of probabilities, p_i, we need to evaluate, making the problem much easier and "cheaper" in computation time. This method has proven to be successful in these intrinsically inefficient detectors [35, 36]

$$R_{click}(N) = 1 - e^{-\eta N} \sum_{i=0}^{m} (1 - p_i) \frac{(\eta N)^i}{i!} \tag{15}$$

We also have to introduce some assumptions to ease the fitting of our data. We will assume that above a certain index k, every probability p_i goes to one ($p_k = 1$ for $k > m$). It's worth noting that we define $p_0 = 0$, so that dark counts are not regarded as 0-photon events. This can be justified by the fact that the dark count rate is independent of the laser repetition rate Ω, and therefore it can not be expressed as a probability per pulse. This QDT method does not make any assumption on how the detector works, but still characterizes its response completely. We will use Equation 2.8 for computing the click probabilty of our detector.

This protocol is a modification of the tomographic procedures designed to handle low efficiency detectors. The method regards absorbed photons ηN instead of input photons N. This dramatically reduces the number of fit parameters needed for systems with low efficiency, i.e. a small value of η. Here, we outline how we compute the tomographic measurements, and what we mean by an *i-photon regime*.

First, we record the count rate R_i and dark count rate D_i during *t* seconds as a function of the optical power P_i. From this data, we also get the standard deviation of both these magnitudes $\sigma_{D,i}$ and $\sigma_{R,i}$. Next, we compute the click probability r_i by subtracting the dark counts from the count rate, and also normalizing to the laser repetition rate Ω .

$$r_i = \frac{R_i - D_i}{\Omega} \tag{16}$$

Our experimental standard deviation is the normalized modulus of the standard deviations of both the count rate and the dark count rate:

$$\sigma_i = \frac{\sqrt{\sigma_{R,i}^2 + \sigma_{D,i}^2}}{\Omega} \tag{17}$$

We compare the obtained σ_i with the theoretical expected deviation of a binomial distribution. For a random process that is attempted Ω t times, with a probability p of success

and probability $q = 1 - p$ of failure, we find a theoretical deviation of:

$$\sigma_i' = \frac{\sqrt{r_i(1 - r_i)}}{\sqrt{\Omega t}} \tag{18}$$

where t is the time used to collect all counts.

As a final step, we convert our optical power data P_i to mean number of photons per pulse using Equation 19

$$N_i = \frac{P_i \lambda}{\Omega h c} \tag{19}$$

where λ is the wavelength in use, h is Planck's constant and c is the speed of light

For the tomography, we evaluate the fit of Equation 2.1 and the goodness of the fit by evaluation the minimum value of the least squares. The click probability depends on the absorption efficiency η, the mean number of photons N_i and an index K, where all probabilities $p_1, ..., p_K$ are all smaller than one, while $p_{K+1}, p_{K+2}, ...$ are equal to one. Therefore, K indicates which of the probabilities $p_k = p_1, p_2, p_3, ..., 1$ are going to have a contribution in the detection events, and which will be set to one (see Section 2.3)

To fit our data we define the least-squares method as:

$$\chi^2(K) = \sum_i \frac{(r_i - p(N_i, \eta, \{p_k\})^2}{\sigma_i^2} \tag{20}$$

Obviously, a model that minimizes χ^2 is desired. At the same time we want to make sure we are not overfitting. In theory, by increasing K, we will always reduce $\chi^2(K)$ at the cost of introducing parameters that may be physically irrelevant. To avoid this issue, we apply model selection through the Akaike Information Criterion (AIC) that penalizes the $\chi^2(K)$ values depending on the number of fit parameters K.

$$AIC = m - 2jln\chi^2(K) = (K + 1) - 2jln\chi^2(K) \tag{21}$$

where m is the number of fit parameters (K+1 in our case) and j is the number of data points (of the shape (N_i,r_i)).

Instead of minimizing $\chi^2(K)$, the quantity AIC is minimized to find an optimum choice for K and the value of $\chi^2(K)$ for that model. It is worth noting that this information criteria only compares the relative goodness of the models, it does not reveal if we are comparing good or bad models for our data.

The effect of noise on the process of tomography

The tomographic fitting is a multi-dimensional non-linear optimization problem, so the effect of different errors is not straightforward. We test the stability of the procedure, by introducing noise in the count rate. The uncertainty in the optical power will only rescale the power axis, but it does not affect the tomography code. Therefore, an error in the count rate is introduced, based on the experimental results of Figure 5.2.

The procedure is the following: we create dummy data using Equation 15 and setting values for η and p_1. To add noise, we follow the result from Figure 5.2 and add a linear error to the values R_i in the dummy data. This function is shown in Figure 5.3, where r is a random number drawn from a normal distribution. Then, this modified data is introduced in the tomography code and we hope to find back the p_1 previously set. This tomography code also requires an initial value for p_1. If we guess p_1 too accurately, the code will always be successful so we choose the guess for p_1 to be a random number r between zero and one. Compared to experimental data, the test data we created has the advantage of knowing the correct value for all p_i beforehand, so we can quantify the error and any possible bias of the tomographic procedure.

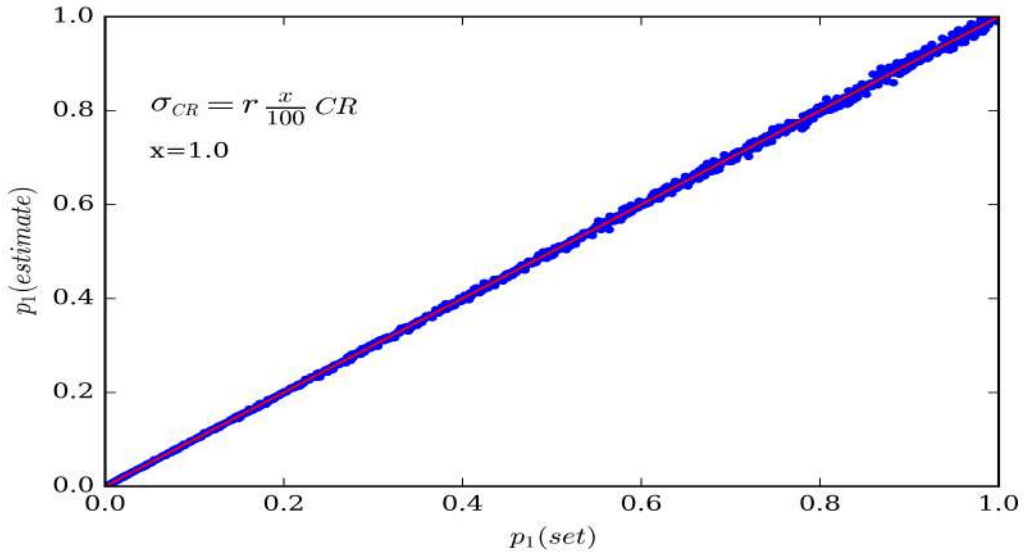

Figure 5.3: Tomography feedback when adding linear noise in the count rate. Estimated values of p_1 are plotted vs. the previously set values, finding a near perfect correlation. Graph provided by E. Abeln.

Figure 5.3 shows the retrieved values of p_1 versus the set values in the test data. The chosen linear error corresponds to 1% of the total count rate, two times the relative error found on Figure 5.2. This shows demonstrates the tomography fitting routine and the model selection are robust for the level of uncertainty present in the experimental results.

Acknowledgments

I would like to thank the University of Leiden and the Quantum Optics group for receiving me and helping me develop my scientific skills. I would also like to thank them for a healthy and diverse work environment. Special appreciation goes to Michiel de Dood for being my supervisor and overall mentor, and to Eduard Abeln, my coworker in this project and partner in all this process. Most importantly, I thank my family for taking care of me, making me who I am today and supporting me in this new experience. I hope this makes you proud, and I will continue to work to be a better myself.

References

[1] C.M. Natarajan, M.G. Tanner, and R.H. Hadfield. Superconducting nanowire single-photon detectors: physics and applications. *Supercond. Sci. Technology*, 25(6):063001, 2012.

[2] D.M. Boroson, J.J. Scozzafava, D.V. Murphy, and B.S. Robinson. 'the lunar laser communication demonstrations (LLCD)'. In *Third IEEE International Conference on Space Mission Challenges for Information Technology*, 2009.

[3] C. M. Natarajan, L. Zhang, H. Coldenstrodt-Ronge, R.H. Hadfield, G. Donati, S.N. Dorenbos, I. Walmsley, and V. Zwiller. Quantum detector tomography of a time-multiplexed superconducting nanowire single-photon detector at telecom wavelenghts. *Optics Express*, 21(1):893–902, 2013.

[4] N. Lusardi, A. Gueraci, R.B.M. Gourgues, J.W.N. Los, and G. Bulgarini. 'array of superconducting nanowire single photon detectors resolving the number of photons in a weak optical pulse'. In *IEEE Nuclear Science Symposium, Medical Imaging Conference and Room-Temperature Semiconductor Detector Workshop*, 2016.

[5] R.H. Hadfield. Single-photon detectors for optical quantum information applications. *Nature Photonics*, 3:696–705, 2009.

[6] F. Marsili, V.B. Verma, J.A. Stern, S. Harrington, et al. Detecting single infrared photons with 93% system efficiency. *Nature Photonics*, 7:210–214, 2013.

[7] V. B. Verma, A.E. Lita, B. Korzh, F.Bussieres, F. Marsili, R.D. Horansky, H. Zbinden M.D. Shaw, R.P. Mirin, and S.W. Nam. High-efficiency WSi superconducting nanowire single-photon detectors operating at 2.5 K. *Appl. Phys. Lett.*, 105(12):122601, 2014.

[8] V. B. Verma, A.E. Lita, M.R. Visser, F. Marsili, D.P. Pappas, R.P. Mirin, and S.W. Nam. Superconducting nanowire single photon detectors fabricated from an amorphous Mo0.75 Ge0.25 thin film. *Appl. Phys. Lett.*, 105(2):022602, 2014.

[9] A. Banerjee, L.J. Baker, A. Doy, M. Nord, R. M. Heath, K. Erotokritou, D. Bosworth, Z.H. Barber, I. MacLaren, and R.H. Hadfield. Characterisation of amorphous molybdenum silicide (MoSi) superconducting thin films and nanowires. *Supercond. Sci. Technology*, 30(8):084010, 2017.

[10] M.Yu. Mikhailov, A.V. Divochiy, A.A. Korneev, and K.V. Smirnov. Superconducting single-photon detector made of MoSi film. *Supercond. Sci. Technology*, 27(9):095012, 2013.

[11] D. Bosworth, S. L. Sahonta, R. H. Hadfield, and Z. H. Barber. Amorphous molybdenum silicon superconducting thin films. *AIP Advances*, 5(8):087106, 2015.

[12] J.S. Lehtinen, A. Kemppinen, E. Mykkänen, M. Prunnila, and A.J. Manninen. Superconducting mosi nanowires. *Supercond. Sci. Technology*, 31(1):015002, 2017.

[13] S.N. Dorenbos, P. Forn-Díaz, T. Fuse, A.H. Verbruggen, T. Zijlstra, T.M. Klapwijk, and V. Zwiller. Low gap superconducting single photon detectors for infrared sensitivity. *Appl. Phys. Lett.*, 98(25):251102, 2011.

[14] C. Schuck, W.H.P. Pernice, and H.X. Tang. Waveguide integrated low noise NbTiN nanowire single-photon detectors with milli-Hz dark count rate. *Nature: Scientific Reports*, 3:1893, 2013.

[15] M. P. van Exter, J.J. Renema, M.J.A de Dood, R. Gaudio, Q. Wang, Z. Zhou, A. Gaggero, F. Mattioli, R. Leoni, D. Sahin, and A. Fiore. Experimental test of theories of the detection mechanism in a nanowire superconducting single photon detector. *Phys. Rev. Lett.*, 112:117604, 2014.

[16] A.D. Semenov, G.N. Gol'tsman, and A.A. Korneev. Quantum detection by current carrying superconducting film. *Physica C: Supercond.*, 351(4):349–356, 2001.

[17] D. Yu. Yodolazov, Yu.P. Korneeva, A.V. Semenov, A.A. Korneev, and G.N. Goltsmann. Vortex assisted mechanism of photon counting in superconducting nanowire single photon detector revealed by external magnetic field. *Phys. Rev. B*, 92(10):104503, 2015.

[18] D. Yu. Yodolazov and A. N. Zotova. Intrinsic detection efficiency of superconducting single photon detector in the modified hotspot model. *Supercond. Sci. Technology*, 27(12):125001, 2014.

[19] K. Suzuki, S. Shiki, M. Ukibe, M. Koike, S. Miki, Z. Wang, and Masataka Ohkubo. Hot-spot detection model in superconducting nano-stripline detector for keV ions. *Appl. Phys. Express*, 4(8):083101, 2011.

[20] Y. Korneeva, I. Florya, S. Vdovichev, M. Moshkova, N. Simonov, N. Kaurova, A. Korneev, and G.N. Goltsmann. Comparison of hot spot formation in NbN and MoN thin superconducting films after photon absorption. *IEEE Trans. Appl. Supercond.*, 27(4):1–5, 2017.

[21] L. N. Bulaevskii, M. J. Graf, and V. G. Kogan. Vortex-assisted photon count and their magnetic field dependence in single-photon superconducting detectors. *Phys. Rev. Lett. B*, 85(1):014505, 2012.

[22] A. Engel, J.J. Renema, K. Ilin, and A. Semenov. Detection mechanism of superconducting nanowire single-photon detectors. *Supercond. Sci. Technology*, 28(11):114003, 2015.

[23] G.N. Goltsmann, O. Okunev, G. Chulkova, A. Lipatov, A. Semenov, K. Smirnov, B. Voronov, and A. Dzardanov. Picosecond superconducting single-photon optical detector. *Appl. Phys. Lett.*, 79:705, 2001.

[24] S Kubo. Superconducting properties of amorphous MoX (X=Si, Ge) alloy films for Abrikosov vortex memory. *J. Appl. Phys.*, 63(6):2033, 1988.

[25] M. Caloz, B. Korzh, N. Timoney, M. Weiss, Stefano Gariglio, R. J. Warburton, C. Schönenberger, J.J. Renema, H. Zbinden, and F. Bussieres. Optically probing the detection mechanism in a molybdenum silicide superconducting nanowire single-photon detector. *Appl. Phys. Lett.*, 110(8):083106, 2017.

[26] J.J. Renema. *The physics of nanowire superconducting single-photon detectors*. PhD thesis, Leiden University, 2015.

[27] R.H. Hadfield, P.A. Dalgarno, J.A. O'Connor, E. Ramsay, R.J. Warburton, E.J. Gansen, M.J. Stevens B. Baek, R.P. Mirin, and S.W. Nam. 7 submicrometer photoresponse mapping of nanowire superconducting single-photon detectors. *Appl. Phys. Lett.*, 91:241108, 2007.

[28] Z. Zhou. *Multi-photon detection with superconducting nanowires*. PhD thesis, Eindhoven Technical University, 2014.

[29] A. J. Kerman, E.A. Dauler, W.E. Keicher, J.K.W. Yang, K.K. Berggren, G.N. Goltsmann, and B. Voronov. Kinetic-inductance-limited reset time of superconducting nanowire photon counters. *Appl. Phys. Lett.*, 88(11):111116, 2006.

[30] Kinetic Inductance. Kinetic inductance — Wikipedia, the free encyclopedia, 2010. [Online; accessed 31-December-2017].

[31] A. J. Annunziata, O. Quaranta, D.F. Santavicca, A. Casaburi, L. Frunzio, M. Ejrnaes, M.J. Rooks, R. Cristiano, S. Pagano, A. Frydman, and D.E. Prober. Reset dynamics and latching in niobium superconducting nanowire single-photon detectors. *J. Appl. Phys.*, 108(8):084507, 2010.

[32] L.M. Artiles, R.D. Gill, and M.I. Guta. An invitation to quantum tomography. *J. Royal Stat. Soc., Series B*, 67(1):109–134, 2004.

[33] A. Feito, J.S. Lundeen, H. Coldenstrodt-Ronge, J. Eisert, M.B. Plenio, and I.A. Walmsley. Measuring measurement: Theory and practice. *New J. Phys.*, 11:093038, 2009.

[34] J.S. Lundeen, A. Feito, H. Coldenstrodt-Ronge, K.L. Pregnell, Ch. Solberhorn, T.C. Ralph, J. Eisert, M.B. Plenio, and I.A. Walmsley. Tomography of quantum detectors. *Nature Physics*, 5:27–30, 2009.

[35] J.J. Renema, M.J.A de Dood, G. Frucci, Z. Zhou, F. Mattioli, A. Gaggero, R. Leoni, A. Fiore, and M.P. van Exter. Modified detector tomography technique applied to a superconducting multiphoton nanodetector. *Optics Express*, 20(3):2806–13, 2012.

[36] M. K. Akhlaghi, A. H. Majed, and J. S. Lundeen. Nonlinearity in single photon detection: Modeling and quantum tomography. *Optics Express*, 19(22):21305–21312, 2011.

[37] Q. Wang. *The physics of nanowire superconducting single-photon detectors*. PhD thesis, Casimir PhD Leiden-Delft, 2015.

[38] A. Nigro and G. Nobile. Electrical resistivity of polycrystalline niobium nitride films. *Phys. Rev. Lett. B*, 37(8):3970, 1988.

[39] J.H. Tyan and J.T. Lue. Grain boundary scattering in the normal state resistivity of superconducting NbN thin films. *J. Appl. Phys.*, 75(1):325, 1994.

[40] J.H. Mooij. Electrical conduction in concentrated disordered transition metal alloys. *Phys. Stat. Sol. A*, 17(2):521–530, 1973.

[41] Y. Imry. *Introduction to Mesoscopic Physics*. Oxford University Press, 1997.

[42] M.J.A. de Dood, J.J. Renema, Q. Wang, R. Gaudio, I. Komen, K.P.M. Hoog, D. Sahin, A. Schilling, M.P. van Exter, A. Fiore, and A. Engel. Position-dependent Local Detection Efficiency in a Nanowire Superconducting Single-Photon Detector. *Nano Lett.*, 15(7):4541–4545, 2015.

[43] R. Lusche, A. Semenov, K. Ilin, M. Siegel, Y. Korneeva, A. Trifonov, A. Korneev, G.N. Goltsmann, D. Yodolazov, and H.W. Hübers. Effect of the wire width on the intrinsic detection efficiency of superconducting-nanowire single-photon detectors. *Journal of Appl. Phys.*, 116(4):043906, 2013.

[44] M. J. A. de Dood, Q. Wang, J.J. Renema, and A. Engel. Design of NbN superconducting nanowire single photon detectors with enhanced infrared photon detection efficiency. *Phys. Rev. Appl.*, 8(3):034004, 2017.

[45] J.J. Kitaygorsky. *Photon and Dark Counts in NbN Superconducting Single-Photon Detectors and Nanostripe*. PhD thesis, University of Rochester, 2008.

[46] K. Harada, O. Kamimura, H. Kasai, T. Matsuda, A. Tonomura, and V.V. Moshchalkov. Direct observation of vortex dynamics in superconducting films with regular arrays of defects. *Science*, 274(5290):1167–1170, 1996.

[47] J. J. Renema, R.J. Rengelink, I. Komen, Q. Wang, R. Gaudio, K.P.M. Hoog, Z. Zhou, D. Sahin, A. Fiore, P. Kes, J. Aarts, M.P. van Exter, M.J.A de Dood, and E.F.C Driessen. The effect of magnetic field on the intrinsic detection efficiency of superconducting single-photon detectors. *Appl. Phys. Lett.*, 106(9):092602, 2015.

[48] D. van Otterloo. *High energy photon detection using a NbN superconducting single-photon detector*. PhD thesis, Leiden University, 2017.